

THE SLOAN DIGITAL SKY SURVEY REVERBERATION MAPPING PROJECT: POST-STARBURST SIGNATURES IN QUASAR HOST GALAXIES AT $z < 1$

YOSHIKI MATSUOKA^{1,2}, MICHAEL A. STRAUSS², YUE SHEN^{3,4,†}, WILLIAM N. BRANDT^{5,6,7}, JENNY E. GREENE²,
 LUIS C. HO^{3,8}, DONALD P. SCHNEIDER^{5,6}, MOUYUAN SUN^{5,6,9}, JONATHAN R. TRUMP^{5,6,†}

Draft version August 21, 2015

ABSTRACT

Quasar host galaxies are key for understanding the relation between galaxies and the supermassive black holes (SMBHs) at their centers. We present a study of 191 broad-line quasars and their host galaxies at $z < 1$, using high signal-to-noise ratio (SNR) spectra produced by the Sloan Digital Sky Survey Reverberation Mapping project. Clear detection of stellar absorption lines allows a reliable decomposition of the observed spectra into nuclear and host components, using spectral models of quasar and stellar radiations as well as emission lines from the interstellar medium. We estimate age, mass M_* , and velocity dispersion σ_* of the host stars, the star formation rate (SFR), quasar luminosity, and SMBH mass M_\bullet , for each object. The quasars are preferentially hosted by massive galaxies with $M_* \sim 10^{11} M_\odot$ characterized by stellar ages around a billion years, which coincides with the transition phase of normal galaxies from the blue cloud to the red sequence. The host galaxies have relatively low SFRs and fall below the main sequence of star-forming galaxies at similar redshifts. These facts suggest that the hosts have experienced an episode of major star formation sometime in the past billion years, which was subsequently quenched or suppressed. The derived $M_\bullet - \sigma_*$ and $M_\bullet - M_*$ relations agree with our past measurements and are consistent with no evolution from the local Universe. The present analysis demonstrates that reliable measurements of stellar properties of quasar host galaxies are possible with high-SNR fiber spectra, which will be acquired in large numbers with future powerful instruments such as the Subaru Prime Focus Spectrograph.

Subject headings: galaxies: active — galaxies: evolution — galaxies: nuclei — galaxies: stellar content — quasars: general — quasars: supermassive black holes

1. INTRODUCTION

Over the last few decades, it has become clear that supermassive black holes (SMBHs) are ubiquitous at galaxy centers throughout the Universe. Stellar or gaseous motions at galactic centers indicate that almost every galaxy bulge in the local Universe harbors a SMBH (e.g., Dressler 1989; Kormendy 1993; Magorrian et al. 1998). The correlation between SMBH mass (M_\bullet) and the stellar velocity dispersion (σ_*) or mass of the bulges (e.g., Merritt & Ferrarese 2001; McLure & Dunlop 2002; Häring & Rix 2004; Gültekin et al. 2009) suggests that the two coevolve, or at least strongly influence each other. The observed scatter in the $M_\bullet - \sigma_*$ relation is remarkably small (Ferrarese & Merritt 2000; Gebhardt et al.

2000). This situation may require a fine-tuning process, which is perhaps a combination of internal physics within galaxies or dark halos and mass averaging via frequent mergers (see the recent review by Kormendy & Ho 2013, and references therein). Beyond the local Universe, SMBHs are known to exist even at very high redshifts. Recent wide-field surveys have discovered more than 40 quasars at $z > 6$ (e.g., Fan et al. 2006; Jiang et al. 2009; Willott et al. 2010; Bañados et al. 2014), with the most distant discovery at $z = 7.1$ (Mortlock et al. 2011). The estimated SMBH mass exceeds $M_\bullet = 10^9 M_\odot$ in many cases (e.g., Jiang et al. 2007; Wu et al. 2015), which has initiated intense discussion on the process of their formation and evolution in the short time scales of the early Universe (e.g., Ferrara et al. 2014; Madau et al. 2014). The $M_\bullet - \sigma_*$ relation of these objects tend to be offset toward higher M_\bullet compared to the local relation at fixed σ_* (e.g., Wang et al. 2010), but possible biases in sample selection and measurements complicate the interpretation (see, e.g., Schulze & Wisotzki 2011; Shen 2013).

Since the Soltan (1982) argument and the latest observations suggest that the local SMBHs have acquired most of their mass during an active galactic nucleus (AGN) phase (e.g., Yu & Tremaine 2002; Marconi et al. 2004; Brandt & Alexander 2015; Comastri et al. 2015), a key to understanding SMBH growth and the origin of the $M_\bullet - \sigma_*$ relation may be found in observational properties of AGNs. One of the outstanding issues is the nature of their host galaxies; in which galaxies do AGNs occur, and what impact do they have on the galaxies? These questions have been addressed by numerous studies in re-

¹ National Astronomical Observatory of Japan, Mitaka, Tokyo 181-8588, Japan; yk.matsuoka@nao.ac.jp

² Princeton University Observatory, Peyton Hall, Princeton, NJ 08544, USA

³ Kavli Institute for Astronomy and Astrophysics, Peking University, Beijing 100871, China

⁴ Carnegie Observatories, 813 Santa Barbara Street, Pasadena, CA 91101, USA

⁵ Department of Astronomy & Astrophysics, The Pennsylvania State University, University Park, PA 16802, USA

⁶ Institute for Gravitation & the Cosmos, The Pennsylvania State University, University Park, PA 16802, USA

⁷ Department of Physics, The Pennsylvania State University, University Park, PA 16802, USA

⁸ Department of Astronomy, School of Physics, Peking University, Beijing 100871, China

⁹ Department of Astronomy and Institute of Theoretical Physics and Astrophysics, Xiamen University, Xiamen, Fujian 361005, China

† Hubble Fellow

cent years, especially in terms of negative feedback effects of AGNs on the star formation rates (SFRs) of the host galaxies. It has been suggested that the energy and/or momentum input of AGNs, which may be triggered along with starbursts by interactions/mergers of gas-rich galaxies (e.g., Barnes & Hernquist 1991), could suppress star formation by expelling the cold gas from galaxies (e.g., Di Matteo et al. 2005; Springel et al. 2005) and/or heating the gas in dark halos (e.g., McNamara & Nulsen 2007). Indeed, recent observations of AGN-driven gas outflows on small scales (e.g., Pounds et al. 2003; Trump et al. 2006; Ganguly et al. 2007; Reeves et al. 2009; Tombesi et al. 2010; Gofford et al. 2013) as well as large scales (e.g., Nesvadba et al. 2006; Feruglio et al. 2010; Greene et al. 2011; Cano-Díaz et al. 2012; Liu et al. 2013a,b) and extended emission-line regions photoionized by AGNs (e.g., Fu & Stockton 2009; Husemann et al. 2010; Matsuoka 2012; Keel et al. 2012) strongly suggest that AGNs have a significant impact on their host galaxies. The idea of negative AGN feedback is also favored because it may provide a solution to longstanding problems with galaxy formation models; for example, it is currently the most compelling process to reconcile the quite different shapes of the dark halo mass function predicted in the Λ CDM cosmology and the observed galaxy stellar mass function at the high mass end (e.g., Bower et al. 2006; Croton et al. 2006; Somerville et al. 2008; Davé et al. 2011; Choi & Nagamine 2011). The AGN feedback may have two distinct modes, i.e., quasar mode and radio mode, which become efficient at different phases of SMBH growth and galaxy evolution (see, e.g., Fabian 2012).

There have been a number of studies on host galaxies of various AGN classes. Different types of AGNs may play different roles in galaxy evolution (e.g., Hickox et al. 2009; DiPompeo et al. 2014, 2015), hence it is crucial to understand the entire AGN and host populations. Elitzur (2012) pointed out that optically-classified narrow-line AGNs are more likely found in dusty circumnuclear environments than are broad-line AGNs (see also Netzer 2015). In a merger-driven scenario of galaxy and SMBH co-evolution (Hopkins et al. 2006), a major merger first creates the dusty starburst/AGN phase observed as luminous infrared galaxies, and then evolves into the dust-free phase observed as optically-luminous quasars (see also Sanders et al. 1988). Therefore, AGNs selected at different wavelengths may have fundamentally different host properties; for instance, dusty infrared-selected AGNs (e.g., Lacy et al. 2013) may be associated with more active star formation on average than are optically-selected AGNs.

Early studies on this subject (e.g., Boroson & Oke 1982; Kotilainen & Ward 1994; Rönnbäck et al. 1996; Bahcall et al. 1997; McLure et al. 1999; Kirhakos et al. 1999; Dunlop et al. 2003; Jahnke et al. 2004, 2007) have shown that host galaxies of optically-luminous AGNs are not a random subsample of normal galaxies. Instead, these AGNs were found to reside in luminous galaxies with young stars and a higher than usual fraction of close companions or tidal features. It has also been suggested that the host galaxies have a substantial contribution from intermediate-age stars (e.g., Canalizo & Stockton 2013), which may correspond to the late stage of accretion episode predicted in the above merger-driven evolutionary scenario. Recent studies have taken advantage of

a large sample of obscured AGNs, which show no visible sign of accretion-disk emission or broad lines at ultraviolet (UV) to optical wavelengths, discovered in large spectroscopic surveys (e.g., Kauffmann et al. 2003; Zakamska et al. 2003; Hao et al. 2005; Reyes et al. 2008) or X-ray observations (e.g., Nandra et al. 2007; Georgakakis et al. 2008; Silverman et al. 2008; Mullaney et al. 2012). Dust extinction serves as a natural coronagraph in these objects and makes analysis of the host galaxies much easier than in unobscured populations. Overall, these studies have statistically confirmed the earlier findings and shown that obscured AGNs reside preferentially in massive galaxies. While there have been controversies over the host colors, recent work points out the importance of using a mass-matched control sample of inactive galaxies for unbiased measurements. Once the mass dependence is properly accounted for, the AGN fraction is more or less constant across the host colors or moderately enhanced in bluer galaxies (e.g., Silverman et al. 2009; Xue et al. 2010; Hainline et al. 2012; Rosario et al. 2013; Trump et al. 2015). At the same time, it has been demonstrated that the color by itself may not be a good tracer of the star-forming properties of the host galaxies (e.g., Cardamone et al. 2010; Rosario et al. 2013).

As a complementary effort to the studies of obscured AGNs in large contemporary surveys, we are investigating the host galaxies of “classical” broad-line quasars selected at optical wavelengths. In our previous work (Matsuoka et al. 2014a), we analyzed the images of about 1,000 Sloan Digital Sky Survey (SDSS; York et al. 2000; Eisenstein et al. 2011) broad-line quasars at $z < 0.6$ and explored their host properties. Deep co-added SDSS images of the Stripe 82 region (Annis et al. 2014) in five bands (u , g , r , i , and z ; Fukugita et al. 1996) were used for the analysis. We developed a technique to decompose spatially a quasar image into nuclear and host components, using the point spread function (PSF) and Sérsic (1968) models, and measured the colors and stellar masses of the host galaxies. We showed that the quasars are hosted exclusively by massive galaxies and that these host galaxies are considerably bluer than the red sequence, showing stark contrast to the color-magnitude diagram (CMD) of inactive galaxies (see also Trump et al. 2013). We also found a positive correlation between M_{\bullet} and stellar mass M_* , but the relation is offset toward large M_{\bullet} compared to the local relation at fixed M_* . While this result could indicate that SMBHs grow earlier than do the host galaxies, we deferred a definitive conclusion until observational biases are fully understood (e.g., Schulze & Wisotzki 2011; Shen 2013).

In this paper, we present the results of a spectral decomposition analysis of SDSS broad-line quasars at $z < 1$. By making use of the high signal-to-noise ratio (SNR) spectra produced by the SDSS Reverberation Mapping (RM) project (see the following section), we measure the spectral properties of about 200 quasar host galaxies and explore their nature. This paper is organized as follows. The data and sample are presented in §2. §3 describes the technique used to decompose a quasar spectrum into nuclear and host components, and the associated error assessments. The main results appear in §4 and are discussed in context of galaxy and SMBH evolution in §5. The summary follows in §6. The cosmological parameters $H_0 = 70 \text{ km s}^{-1} \text{ Mpc}^{-1}$,

$\Omega_M = 0.3$, and $\Omega_\Lambda = 0.7$ are used throughout this work. All magnitudes are presented on the AB system (Oke & Gunn 1983).

2. DATA ACQUISITION AND BASIC PROCESSING

We use the data acquired in the SDSS-RM project, in which a single spectroscopic field was repeatedly observed to explore the variability of quasars. The full technical details of the project are found in Shen et al. (2015a), and hence we repeat only the most relevant aspects here. SDSS-RM was conducted during the dark/grey time in the final season (2013–2014) of the SDSS-III Baryon Oscillation Spectroscopic Survey (BOSS; Dawson et al. 2013) following its early completion due to unexpectedly good weather. The target field (centered at $\alpha_{J2000} = 14^{\text{h}}14^{\text{m}}49^{\text{s}}.00$, $\delta_{J2000} = +53^{\circ}05^{\text{m}}00^{\text{s}}.0$) coincides with the Panoramic Survey Telescope & Rapid Response System 1 (Pan-STARRS 1; Kaiser et al. 2010) Medium Deep Field MD07 which lies within the Canada-France-Hawaii Telescope Legacy Survey W3 field. About 1,000 spectroscopically confirmed quasars are known in this 7-deg² field from SDSS-I/II and SDSS-III, most of which were targeted by the BOSS spectroscopy. Additional quasars have been identified by the DEEP2 Galaxy Redshift Survey (Newman et al. 2013) and by follow-up spectroscopy of Pan-STARRS 1 variable sources (P. J. Green et al., in preparation). The redshifts of these quasars have been determined by matching identified emission lines with a pre-defined line list or by cross correlating observed spectra with spectral templates.

The SDSS-RM quasars were selected as a flux-limited sample of 849 objects at $i < 21.7$ mag, with objects in fiber collisions being removed. Each quasar is labelled with an identification number RMID. We stress that the entire sample is composed of spectroscopically-confirmed broad-line quasars, the vast majority of which were selected at optical wavelengths; further details of the sample selection are given in §3.1 of Shen et al. (2015a). The quasars follow the luminosity-redshift distribution expected from the luminosity function estimates in Hopkins et al. (2007), suggesting that the sample is fairly uniformly selected above the adopted flux limit. Figure 1 displays the distribution of their redshifts and absolute magnitudes in SDSS i band (M_i). M_i was derived from the SDSS PSF magnitudes, k -corrected to $z = 0$ with the correction factors taken from Richards et al. (2006). The quasars analyzed in this work ($z < 1$; see §3.2) have luminosities comparable to or lower than the classical quasar threshold $M_B = -23$ mag (Schmidt & Green 1983), which corresponds to $M_i \simeq -23$ mag assuming the SDSS quasar composite spectrum of Vanden Berk et al. (2001) and correcting for the different cosmology used in Schmidt & Green (1983).

The SDSS-RM observations were carried out with the BOSS spectrograph (Smee et al. 2013) mounted on the SDSS 2.5-m telescope (Gunn et al. 2006) in 32 epochs from January to July 2014. The spectrograph provides wavelength coverage from $\lambda = 3,650$ to $10,400$ Å with a spectral resolution of $R \sim 2,000$. The BOSS plates allow 1,000 fibers of $2''$ diameter to be observed simultaneously; the fibers were allocated to the 849 quasars, 70 standard stars, a luminous red galaxy (required by the BOSS targeting algorithm), and 80 sky positions. A typ-

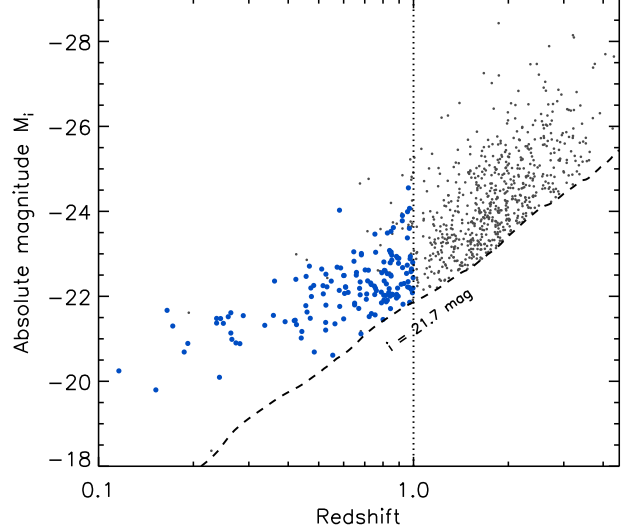


FIG. 1.— Redshifts and i -band absolute magnitudes of the 849 SDSS-RM quasars (small and large dots), defined by the flux limit $i < 21.7$ mag (dashed line). We analyze 191 quasars at $z < 1.0$ (dotted line) in this study. Our final sample consists of 156 quasars (large dots) with successful spectral decomposition (see §3.2).

ical epoch consists of eight to ten 15-minute exposures, totaling 65 hours when summed over the 32 epochs. The data were first processed through the BOSS spectroscopic pipeline `idlspec2d v5_7_1`, which performs flat-fielding, 1d extraction, wavelength calibration, sky subtraction, and flux calibration (Bolton et al. 2012, and references therein). The spectrum was resampled to a pixel scale of 69 km s^{-1} , which corresponds to roughly a half of the resolution element. The flux calibration is tied to the PSF magnitudes of standard stars in the plate. These pipeline-processed data were released to the public in the SDSS data release (DR) 12 (Alam et al. 2015). The spectrophotometry was further improved with a custom flux-calibration algorithm; SDSS-RM observed 3.5 times more standard stars per plate than the main BOSS survey, which enabled us to trace the spatial variation of the calibration more precisely (Shen et al. 2015a). Later in this work, we apply an additional aperture correction so that the decomposed host magnitude represents the total galaxy light. The data of all epochs were stacked by inverse-variance weighted mean to create high SNR spectra, which are used throughout this work. The SNR of the stacked spectra range from ~ 5 to ~ 300 per pixel, with the median value of ~ 30 . The pixel flux errors were taken from the BOSS pipeline and properly propagated throughout the post-processing. We corrected the spectra for Galactic dust extinction with the extinction curve of Pei (1992) and the color excess E_{B-V} taken from Schlegel et al. (1998).

3. DATA ANALYSIS

We describe the details of the data analysis in this section. In §3.1, we introduce our spectral decomposition technique which separates the galaxy component from an observed quasar spectrum. This method is applied to the SDSS-RM data in §3.2. In §3.3, we evaluate the reliability of the present method by Monte Carlo simulations and by comparisons with previous measurements.

3.1. Spectral decomposition technique

We aim to extract host-galaxy information from the observed spectra with as little ambiguity as possible. This is a challenge, since different combinations of quasar and stellar spectral models give rise to similar total spectra at UV-to-optical wavelengths. For the present analysis, we choose the rest-frame spectral window from $\lambda = 3700 \text{ \AA}$ to 5400 \AA , which includes a wealth of stellar absorption features as well as important nebular lines such as [O II] $\lambda 3727$, H β , and [O III] $\lambda\lambda 4959, 5007$. We devise a method to apply a series of spectral fits to the data in such a way that degeneracies between model components are minimized. The following models are used to represent the relevant emission components, namely, the quasar accretion disk, gas in the broad line region (BLR), narrow line region (NLR), and interstellar medium (ISM), and stars in the host galaxy.

1. Accretion disk: the emission from the quasar accretion disk can be represented by a single power-law continuum ($f_\lambda \propto \lambda^{\alpha_{\text{pl}}}$) in our spectral window, with the amplitude and slope being free parameters. Previous observations have found slopes spanning the range of $-2.5 < \alpha_{\text{pl}} < 0.0$, with a typical value of $\alpha_{\text{pl}} \simeq -1.5$ (Richstone & Schmidt 1980; Francis 1996; Vanden Berk et al. 2001; Ivezic et al. 2002; Pentericci et al. 2003).

2. Gas in the BLR, NLR, and ISM:

- (a) $3700 \text{ \AA} < \lambda < 4450 \text{ \AA}$: numerous high-order Balmer lines and metal lines as well as the Balmer continuum make up a pseudo-continuum in this spectral region. It is modeled by subtracting the power-law contribution from the SDSS quasar composite spectrum provided by Shen et al. (2011). We take the composite of the highest-luminosity bin ($L_{5100} = 10^{45.5} \text{ erg s}^{-1}$) so that the host contamination is minimized; Shen et al. (2011) report that the contamination at $\lambda = 5100 \text{ \AA}$ is negligible in a quasar with $L_{5100} > 10^{45.0} \text{ erg s}^{-1}$. The power-law contribution is determined in two continuum windows (in which strong emission lines are absent) at $\lambda = 4200 - 4230$ and $5470 - 5500 \text{ \AA}$. This pseudo-continuum template also includes individual BLR, NLR, and ISM lines present in the original composite spectrum, although the ISM contribution should be minimal at this highest quasar luminosity. We consider seven additional narrow lines or line complexes, namely, [O II] $\lambda 3727$, [Fe VII] $\lambda 3760$, [Ne III] $\lambda 3870$, He I + H8 $\lambda 3890$, [Ne III] $\lambda 3969$, H δ , and H γ , to fit the ISM lines. They are each modeled with Gaussian profiles sharing the same velocity dispersion (σ_g) and velocity offset relative to the object's formal redshift (v_g^{off}), both of which are free parameters.
- (b) $4450 \text{ \AA} < \lambda < 5400 \text{ \AA}$: the dominant contributors to this spectral region are the Fe II pseudo-continuum, H β , and [O III] $\lambda 4959, \lambda 5007$ lines. We use the empirical Fe II

template of Véron-Cetty et al. (2004) created from an observed spectrum of I Zw 1, a prototype narrow-line Seyfert 1 galaxy (e.g., Osterbrock & Pogge 1985). This template is velocity-broadened with a Gaussian kernel with $\sigma_{\text{FeII}} = 1,500 \text{ km s}^{-1}$; we test a different value of σ_{FeII} later. H β is modeled with three Gaussian emission profiles with variable amplitudes, widths, and velocity offsets, while the two [O III] lines are each modeled with two Gaussians. The widths of these lines are varied independently from those of the above ISM lines. We assume that the two [O III] lines have the theoretical intensity ratio $\lambda 5007/\lambda 4959 = 3.0$ and that the two lines share the same profile (i.e., widths and velocity offsets).

3. Stars: we use simple stellar population (SSP) models of Maraston & Strömbäck (2011) to represent the stellar emission. SSP is a single generation of stars formed in an instantaneous starburst; it is the simplest assumption for a stellar population and is suitable for the present analysis, in which the dominant quasar light makes it difficult to exploit full details of the stellar properties. We test more complicated stellar population models in §3.3. For SSP models, we adopt the STELIB (Le Borgne et al. 2003) stellar spectral library, the Chabrier (2003) initial mass function (IMF), and solar metallicity. Stellar age (t_*) takes values from 30 Myr to the age of the Universe at the redshift of each object. The SSP spectra are velocity-broadened in accordance with the stellar velocity dispersion (σ_*) and the instrumental resolution¹¹ assumed to be $\sigma_{\text{inst}} = 65 \text{ km s}^{-1}$, and offset in wavelength by v_*^{off} relative to the object's redshift; both σ_* and v_*^{off} are free parameters. The amplitude of the SSP model determines the stellar mass M_* . We test different choices of stellar library, IMF, and metallicity in §4.

Our default models do not incorporate the effect of dust extinction. In fact, the amount of extinction observed in optically-selected broad-line quasars is usually quite small (Richards et al. 2003; Hopkins et al. 2004; Salvato et al. 2009; Matuse et al. 2012) and its effect is limited. Recently Krawczyk et al. (2014) investigated a large sample of SDSS broad-line quasars and found that the vast majority are consistent with $E_{B-V} < 0.1$ mag. Here we assume no dust extinction for both quasar nuclei and host galaxies, and later confirm that non-zero E_{B-V} values have little impact on our qualitative conclusions. We note that there are dust-reddened broad-line quasars which can be identified in the near-infrared, although their surface density is much lower than that of optically-selected quasars (e.g., Glikman et al. 2012). Urrutia et al. (2008) presented an enhanced merger fraction in dust-reddened quasars, hence their host stellar properties may be quite different from those of normal optically-selected quasars.

¹¹ The actual instrumental resolution varies as a function of wavelength, but here we assume the fixed mean value (see Smeeth et al. 2013).

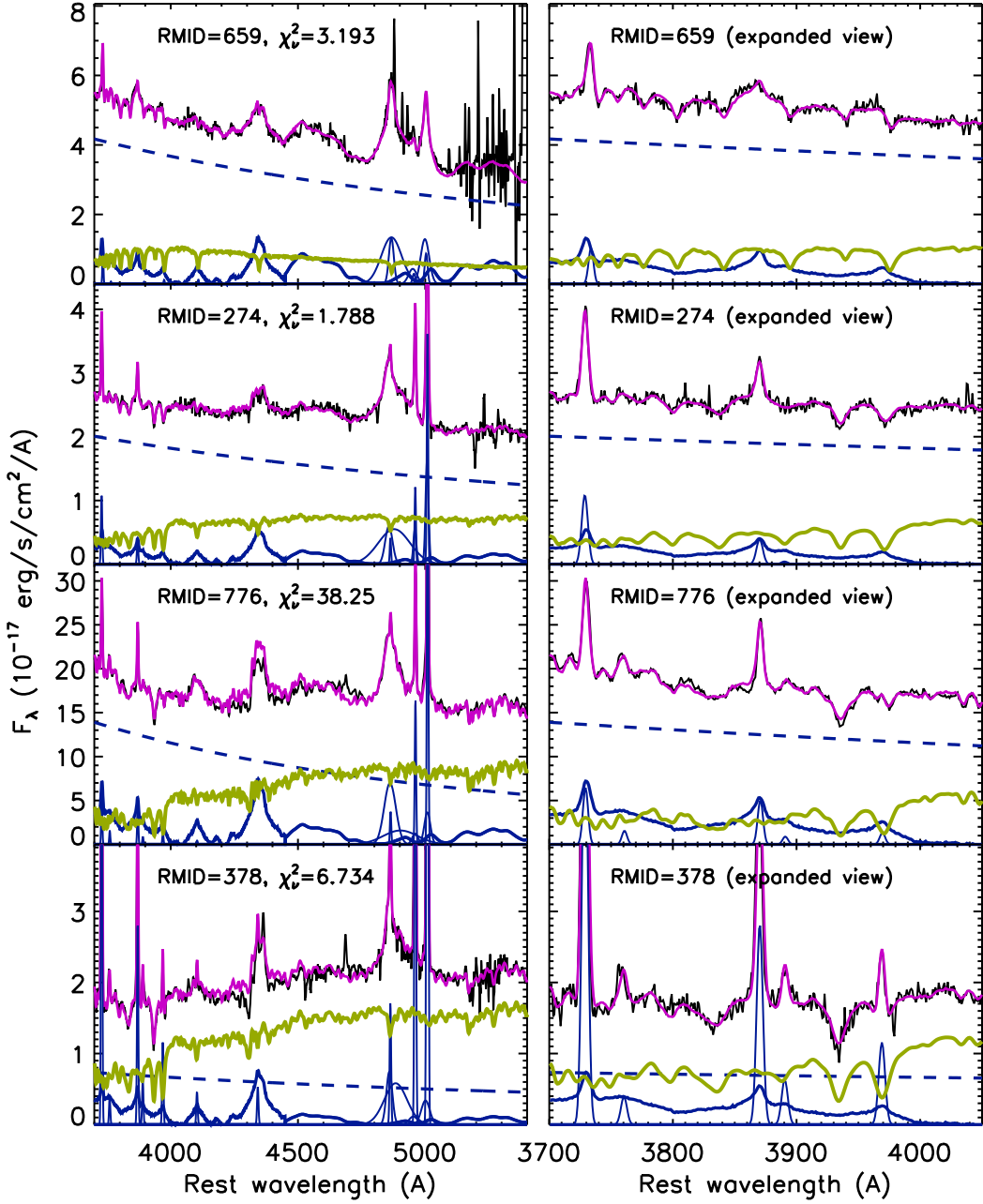


FIG. 2.— Examples of the spectral decomposition. Each row corresponds to a single quasar in the full spectral window (left) and expanded view (right). The first, second, and third rows show objects fitted with young ($t_* = 30$ Myr), intermediate (1 Gyr), and old (8 Gyr) SSP models, respectively, while the last row displays an object with strong narrow ISM emission lines. Black lines indicate the observed co-added spectra, while the red lines show the total model spectra. The other lines represent the individual model components, namely, the quasar power-law continuum (blue dashed), the gas emission from the BLR, NLR, and ISM (blue solid), and the stellar emission (green).

We perform a series of spectral fits rather than fitting all the model components simultaneously. First, we determine the stellar age t_* by fitting the spectrum over the rest-frame wavelength range $\lambda = 3700 - 4050$ Å with the quasar power-law slope fixed to $\alpha_{\text{pl}} = -1.5$. This spectral window is chosen because (i) a wealth of strong stellar absorption features are present, including the Ca HK lines and the 4000 Å break; (ii) the quasar emission is relatively featureless; (iii) the precise value of α_{pl} is not important, since the flux ratio between the two edges of the window (f_{4050}/f_{3700}) changes only by $\sim 10\%$ when α_{pl} varies from -1.5 to the extreme values of 0.0 or -2.5 . Second, the wider spectral range of $\lambda = 3700 - 4750$ Å

and $5050 - 5400$ Å (i.e., the full $3700 - 5400$ Å spectral window excluding the $\text{H}\beta$ region) is fit by varying all parameters but t_* , which is fixed to the value determined above. We then return to the first step and update t_* with the latest α_{pl} . These two steps are iterated until t_* converges, but in most cases the convergence occurs with no more than two iterations. Finally, we subtract the best-fit model from the full spectrum and fit the residual with the $\text{H}\beta$ and $[\text{O III}]$ line models in the range $\lambda = 4750 - 5050$ Å.

3.2. Application to the data

We apply the above algorithm to all the 191 SDSS-RM quasars found at $z < 1$; our spectral window ($\lambda = 3700 - 5400 \text{ \AA}$) is shifted beyond the spectrograph coverage at higher redshifts. The standard χ^2 method is used for the model fitting with the IDL routine MPFIT (Markwardt 2009). As described above, the pixel flux errors were taken from the BOSS spectroscopic pipeline and propagated appropriately through the co-addition process. Figure 2 shows four typical examples of the decomposition results. While the spectra are usually dominated by quasar light, most of the small-scale features are fit by the stellar models. The median reduced χ^2 of the fits over the whole spectral window is about five; as seen in Figure 2, this rather large value is caused by the systematic discrepancy at certain wavelengths between the observed spectra and the models, the latter being not complex enough to provide perfect fits to every emission and absorption feature across the spectrum. The uncertainties in the best-fit parameters are estimated following the Monte Carlo method outlined in Shen et al. (2011). We create 50 mock spectra by adding random noise to the original spectrum, using the Gaussian probability density function (PDF) with the standard deviation equal to the flux error at each pixel, and process them through the decomposition algorithm. The measurement errors are evaluated from the 68 % central intervals of the parameter distributions of the 50 trials. We add additional 20 % error to the derived stellar age, which accounts for the minimum uncertainty arising from non-continuous coverage of ages in the SSP models. We perform further assessment of possible systematic uncertainties in the next section.

Figure 3 presents the histogram of the fractional contribution of the stellar component to the total flux (f_*) measured at $\lambda = 4000 \text{ \AA}$ in the rest frame. We exclude the 31 objects with $f_* < 0.1$ from the following analysis; we will demonstrate in the next section that their host results are unreliable. An additional four objects are excluded because they have particularly large statistical uncertainties in the host stellar mass, $\Delta \log(M_*/M_\odot) > 0.5 \text{ dex}$. These excluded objects tend to have high quasar luminosities, as shown in Figure 1. Our final sample consists of the remaining 156 quasars, more than 80 % of the initial 191 objects. The median redshift and absolute magnitude of the 156 quasars are $\langle z \rangle = 0.72$ and $\langle M_i \rangle = -22.2 \text{ mag}$, respectively.

We focus on six physical quantities in this work, namely, stellar age t_* , stellar mass M_* , SFR, stellar velocity dispersion σ_* , $[\text{O III}] \lambda 5007$ luminosity $L_{[\text{O III}]}$, and SMBH mass M_\bullet . The parameters t_* , M_* , σ_* , and $L_{[\text{O III}]}$ are taken directly from the decomposition results. Since the quantity σ_* is poorly constrained in many cases, its measurement is rejected if the best-fit value lies outside the physically plausible range ($10 < \sigma_* < 400 \text{ km s}^{-1}$) or smaller than three times the estimated statistical error. SFRs are estimated from the $[\text{O II}] \lambda 3727$ luminosity. As shown in Figure 2, the $[\text{O II}]$ line is comprised of two components, i.e., the quasar BLR/NLR template and the host ISM line with Gaussian profile. The former contribution is tied to the overall amplitude of the BLR/NLR template, which is fit over the full spectral window. We use the luminosity of the latter ISM component ($L'_{[\text{O II}]}$)

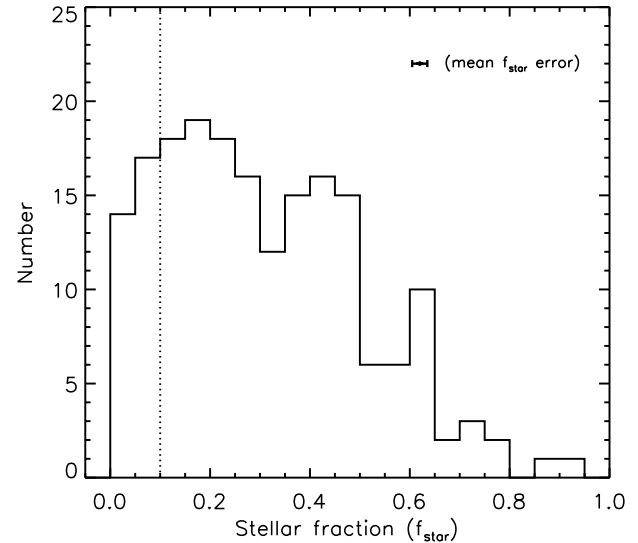


FIG. 3.— Histogram of the fractional stellar contribution to the total flux (f_*), measured at $\lambda = 4000 \text{ \AA}$ in the rest frame, for the 191 SDSS-RM quasars at $z < 1$. The typical f_* uncertainty is shown with the error bar at the top right corner. We deem the decomposition analysis successful for 156 objects (82 % of the initial 191 quasars) with $f_* > 0.1$ (dotted line).

for SFR estimates, assuming the Kennicutt (1998) calibration:

$$\text{SFR} (M_\odot \text{ yr}^{-1}) = (1.4 \pm 0.4) \times 10^{-41} L'_{[\text{O II}]} (\text{erg s}^{-1}). \quad (1)$$

Since the NLR usually contributes only weakly to this low-ionization line, it may be a good tracer of star formation in quasar host galaxies even without spectral decomposition (Ho 2005). On the other hand, Kim et al. (2006) found that the $[\text{O II}]/[\text{O III}]$ ratios observed in SDSS AGNs at $z < 0.3$ are fully consistent with AGN photoionization, hence there is no need to invoke any additional $[\text{O II}]$ source such as star formation. Although the mean quasar contribution is properly subtracted with the BLR/NLR template in this work, we conservatively treat the derived SFRs as rough estimates only, given that our single BLR/NLR template cannot trace object-to-object variation of the $[\text{O II}]$ strength. Another concern is the effect of dust extinction, which we discuss later.

SMBH masses are estimated with the single-epoch virial estimator (Vestergaard & Peterson 2006):

$$\log \left(\frac{M_{\text{BH}}}{M_\odot} \right) = \log \left(\left[\frac{\text{FWHM}(\text{H}\beta)}{1000 \text{ km s}^{-1}} \right]^2 \left[\frac{\lambda L_\lambda(5100 \text{ \AA})}{10^{44} \text{ erg s}^{-1}} \right]^{0.5} \right) + (6.91 \pm 0.02). \quad (2)$$

It is believed that this $\text{H}\beta$ -based estimator is more reliable than other single-epoch estimators, such as those based on $\text{C IV} \lambda 1549$ or $\text{Mg II} \lambda 2800$ (Shen & Liu 2012; Shen 2013). In some cases our $\text{H}\beta$ models apparently fit the underlying continuum residuals rather than the line itself, especially when the SNR around $\text{H}\beta$ is low. The M_\bullet measurements were rejected for 16 such fits identified by visual inspection. We will eventually obtain more precise SMBH masses for all the objects with RM analysis.

The limited aperture size of the BOSS spectrograph

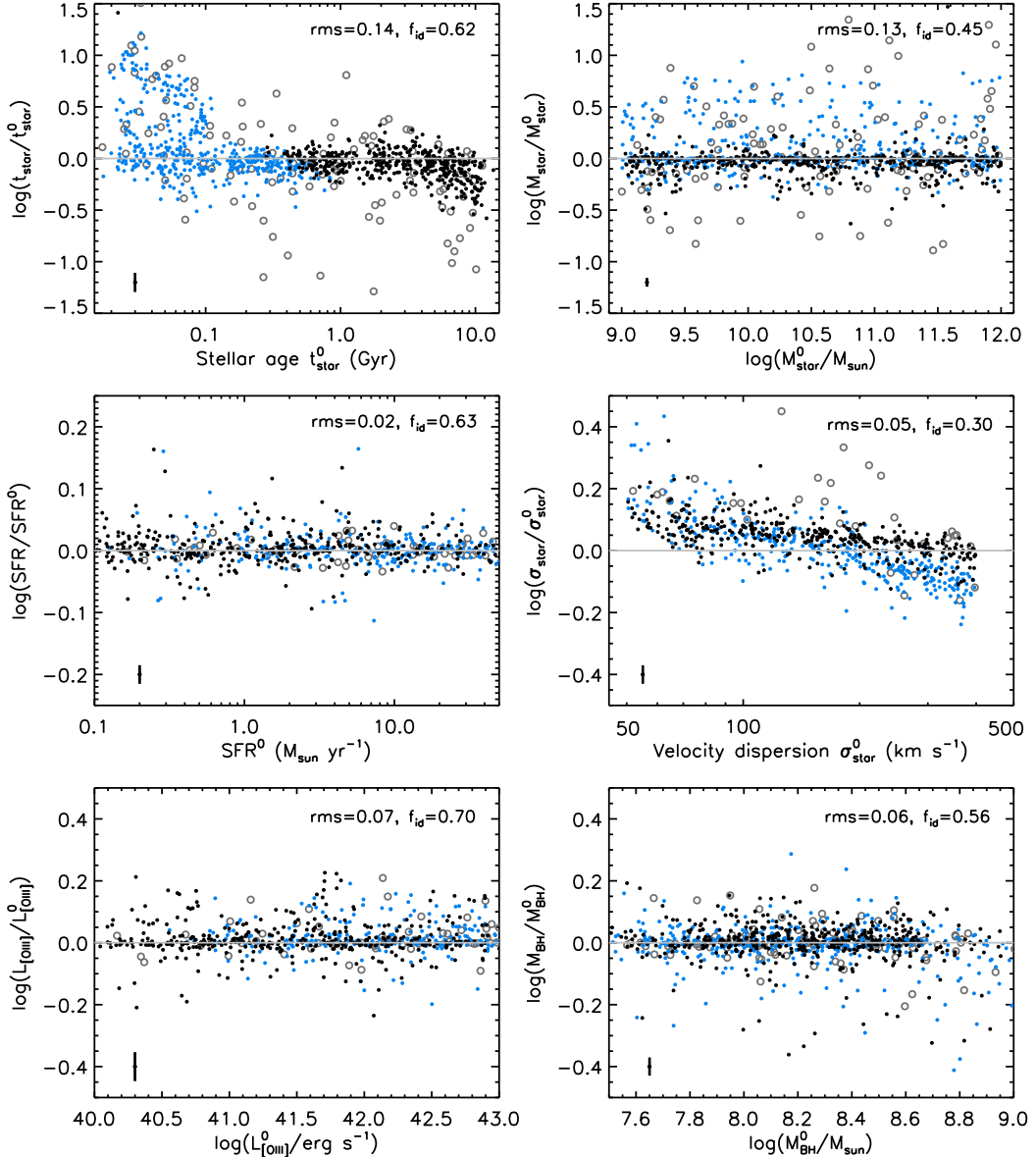


FIG. 4.— Deviations of the measured (output) values from the intrinsic (input; the quantities with the superscript “0”) values for t_* (top left), M_* (top right), SFR (middle left), σ_* (middle right), $L_{\text{[OIII]}}$ (bottom left), and M_{\bullet} (bottom right) for simulated spectra. The black dots represent the spectra with reliable fits of the stellar component (output stellar fraction $f_* > 0.1$, mass error $\Delta \log M_* < 0.5$ dex, and stellar age $t_* > 0.5$ Gyr), while the blue dots represent those with younger stellar ages ($f_* > 0.1$, $\Delta \log M_* < 0.5$ dex, and $t_* < 0.5$ Gyr; we find few such cases in the real quasars as described in the text). The open circles show the remaining spectra with poor fits of the stellar component ($f_* < 0.1$ or $\Delta \log M_* > 0.5$ dex). The symbols in the upper left panel are given small random offsets in stellar age to improve visibility. The typical statistical error is shown by the error bar at the bottom left corner of each panel. The horizontal lines represent the identity lines. The numbers in each panel indicate, for the black dots, the RMS scatter around the identity line and the fraction (f_{id}) of those whose ordinate values are consistent with zero within 1σ statistical error.

fibers does not include all the light from the extended hosts. The fiber diameter of $2''$ corresponds to approximately 14 kpc at the median redshift of our sample ($z = 0.72$). We correct the stellar mass, derived from the decomposed galaxy flux (f_g^{fiber}), for the aperture loss as follows. Since the spectrophotometry of the BOSS spectroscopic pipeline is tied to the PSF magnitude of standard stars, the quasar flux decomposed from each spectrum (f_q) should correctly represent the total flux of the unresolved quasar nucleus. The SDSS imaging pipeline measures the total nuclear plus host flux (f_{tot}) with the `cModel` algorithm (Abazajian et al. 2004), which fits galaxy models to the observed image profile. There-

fore, the total host flux (f_g) is given by $f_g = f_{\text{tot}} - f_q$. Multiplying the stellar mass of each source measured from the spectra by the ratio f_g/f_g^{fiber} provides a crude estimate of the total stellar mass, with the implicit assumptions that the mass-to-luminosity ratio in the fiber represents that in the whole galaxy and that quasar variability between the epochs of imaging (before 2005) and spectroscopic (2014) observations does not introduce a significant bias. This aperture correction is calculated in the observed-frame r band. The correction is not applied to the SFRs, since broad-band magnitudes are a poor tracer of the spatial extent of the [O II] line emission. When we later discuss the relation between SFR

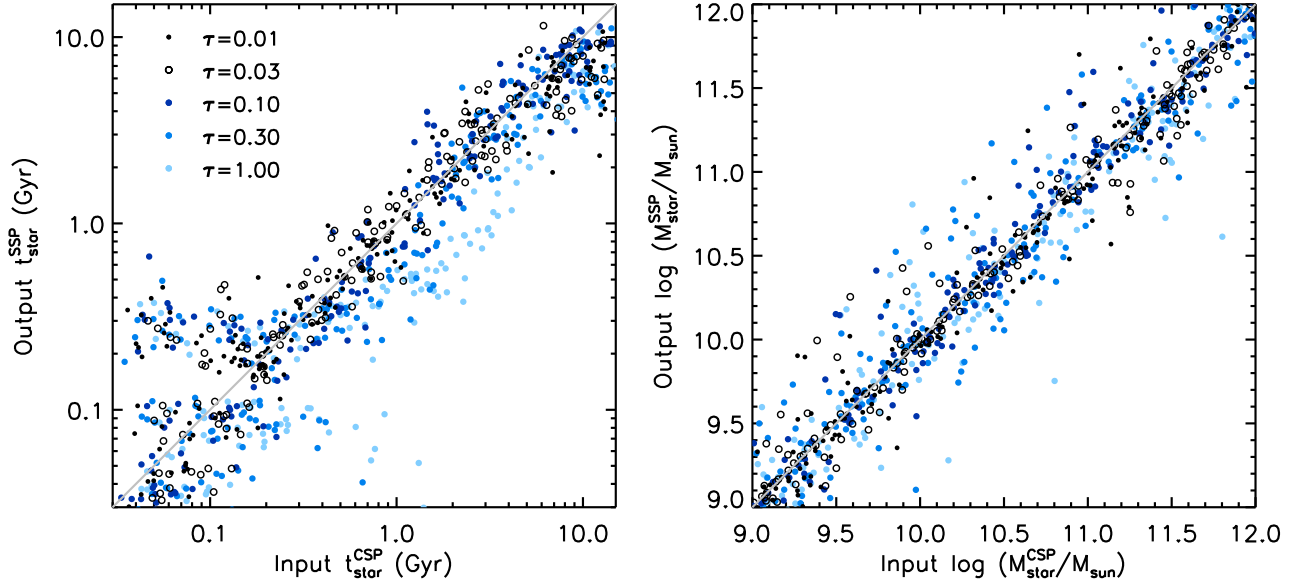


FIG. 5.— Comparison between the input CSP maximum age t_{*}^{CSP} and the output SSP age t_{*}^{SSP} (left) or between the accumulated CSP mass M_{*}^{CSP} and the SSP mass M_{*}^{SSP} (right). The different symbols represent different values of the star formation timescale τ (in units of Gyr) as reported in the left panel. The points in the left panel are given small random offsets to improve visibility. The gap at $t_{*}^{\text{SSP}} \sim 0.15$ Gyr is caused by the sparse time sampling of our SSP models around this age. The diagonal lines represent the identity lines. The quantities t_{*}^{SSP} and t_{*}^{CSP} are largely consistent at $t_{*}^{\text{CSP}} > 0.1$ Gyr and $\tau <$ a few 100 Myr, while t_{*}^{SSP} becomes smaller at larger τ due to the prolonged star formation. There is little systematic offset between the input and output masses.

and stellar mass, we use the stellar mass within the fiber (M_{*}^{fiber} ; the stellar mass before the aperture correction) so that the two quantities refer to the same central part of the galaxies. Therefore, the present analysis does not map SFR and its relation to stellar mass to extended regions of the galaxies outside the fibers.

3.3. Reliability of the present method

Here the reliability of the present method is evaluated with Monte Carlo simulations. We generate 1,000 mock spectra by combining spectral models of quasar accretion disk, gas in the BLR, NLR, ISM, and host stellar population as described in §3.1, with realistic PDFs for the parameter values. The power-law slope α_{pl} is assumed to follow a Gaussian PDF with mean -1.5 and standard deviation 0.3 , which approximately reproduces past measurements (Ivezić et al. 2002; Pentericci et al. 2003). The SSP age is randomly drawn from 14 logarithmically spaced values between $t_{*} = 30$ Myr and 10 Gyr, while the stellar mass is distributed uniformly on a logarithmic scale between $\log(M_{*}/M_{\odot}) = 9$ and 12. The ratio between the mean amplitudes of the stellar model and the quasar power law is assumed to follow a logarithmically-uniform PDF between 0.01 and 10.0. The stellar velocity dispersion is drawn from a logarithmically-uniform PDF between 50 and 400 km s $^{-1}$. All other model parameters are assumed to follow the Gaussian PDFs best describing the distributions derived in our own measurements. For each of the mock spectra, we randomly select a SDSS-RM quasar at $z < 1$ and apply its redshift and pixel flux errors to mimic a real spectrum.

These mock spectra are processed through the decomposition algorithm used for the real data. Figure 4 presents the comparisons between the intrinsic (input) and measured (output) parameter values. The stellar age and mass show relatively large scatter, reflecting the ambiguity in decomposing the nuclear and stel-

lar components from the observed spectra. The scatter is significant at $t_{*}^0 \lesssim 0.1$ Gyr (the superscript “0” represents the input parameter), where the relatively blue spectra of young stars are difficult to distinguish from those of quasar nuclei. These degeneracies result in overestimated ages up to $t_{*} \sim 0.5$ Gyr, hence we conservatively regard measured stellar ages at $t_{*} \leq 0.5$ Gyr as upper limits (although we find only few such cases in the real quasars; see below). At larger ages, most of the scatter is caused by spectra with $f_{*} < 0.1$ or $\Delta \log M_{*} > 0.5$ dex. When these simulated quasars are eliminated, as we did for the real sample, all six parameters are constrained within a scatter of roughly 0.15 dex; the actual RMS scatter of each parameter is reported in each panel of the figure. Figure 4 also reports for each parameter the fraction (f_{id}) of the simulated spectra whose output value is consistent with the input (i.e., the ordinate value is consistent with zero) within 1σ statistical error. The fraction for σ_{*} is low, due to the systematic overestimation of this parameter at small σ_{*}^0 where the measurement is most difficult. For the other five parameters, f_{id} are somewhat smaller than but roughly comparable to the expected 68 %.

We also perform a set of simulations that replace the input SSP models with composite stellar population (CSP) models with exponentially declining star formation history. CSP spectra are calculated as

$$f_{\lambda}(t_{*}^{\text{CSP}}) = \int_0^{t_{*}^{\text{CSP}}} \psi(t_{*}^{\text{CSP}} - t) f_{\lambda}^{\text{SSP}}(t) dt; \psi(t) = e^{-t/\tau}, \quad (3)$$

where t_{*}^{CSP} is the time since the onset of star formation (i.e., the maximum CSP age), $\psi(t)$ is the star formation history with the exponentially declining timescale τ , and $f_{\lambda}^{\text{SSP}}(t)$ is an SSP spectrum. We create 1,000 mock spectra by combining these CSP models with other emission

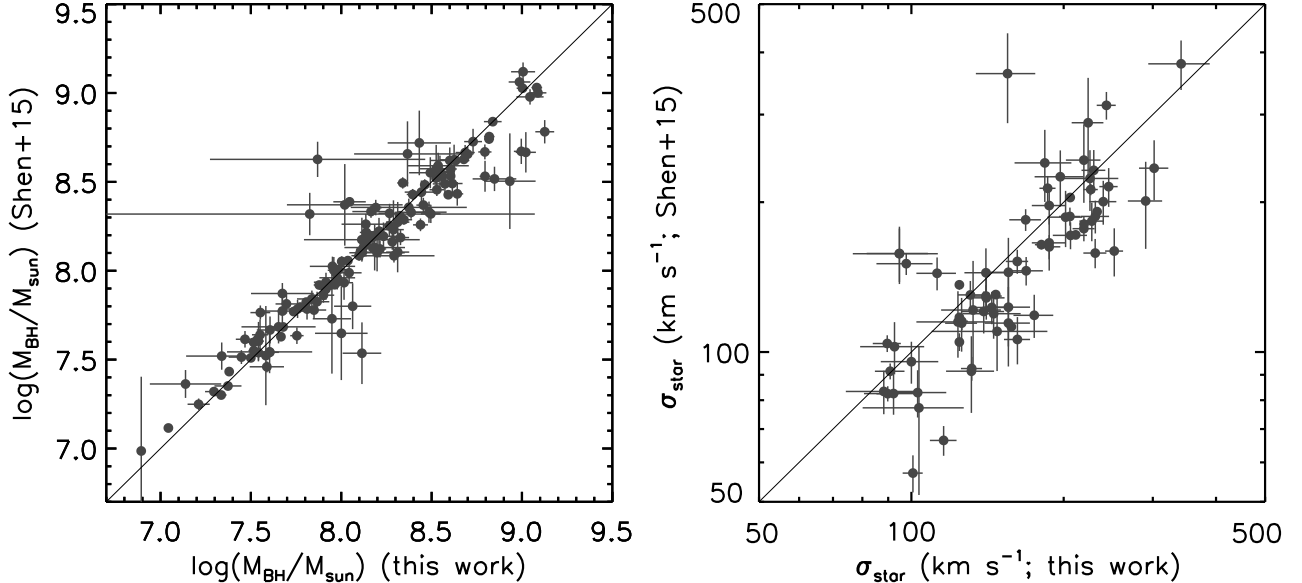


FIG. 6.— Comparison of M_{\bullet} (left; 140 successful measurements) or σ_{*} (right; 73 successful measurements) for common objects measured by Shen et al. (2015b) and this work. The diagonal lines represent the identity lines. The two sets of measurements are in good agreement with each other, although there is a small ($\sim 10 \text{ km s}^{-1}$) systematic offset in σ_{*} .

components as above, and process them through the decomposition algorithm (which uses the SSP models to represent stellar spectra). The results are shown in Figure 5 for stellar age and mass; the other parameters are less sensitive to the choice of star formation history. The decomposition is unreliable for input $t_*^{\text{CSP}} \lesssim 0.1 \text{ Gyr}$, which is similar to the situation described above. At larger t_*^{CSP} , the output SSP age is consistent with t_*^{CSP} when τ is less than a few 100 Myr, while the former becomes systematically small at larger τ due to the prolonged star formation. There is little systematic offset between the output SSP mass and the input CSP mass, the latter being the mass accumulated during the whole star formation history.

Finally, we compare our measurements of M_{\bullet} and σ_{*} with the previous measurements by Shen et al. (2015b), who investigated the $M_{\bullet} - \sigma_{*}$ relation of the SDSS-RM quasars at $z < 1$ using the same co-added spectra as in this work. They performed spectral decomposition with the principal component analysis (PCA) method following Vanden Berk et al. (2006). The PCA method has the advantage of being highly efficient in reproducing observed spectra with an optimal number of empirical eigenspectra, but the interpretation of the reconstructed spectra is usually not straightforward. The SMBH masses were derived with the Vestergaard & Peterson (2006) estimator as in this work, while the stellar velocity dispersion was measured with the `vdispfit` routine in the `idlspec2d` package and with the penalized pixel-fitting code (Cappellari & Emsellem 2004) in the spectral window $\lambda = 4125 - 5350 \text{ \AA}$. Figure 6 compares the M_{\bullet} and σ_{*} values measured by the two studies. They are in good agreement with each other, although there is a slight systematic offset in σ_{*} ; our measurements give $\sim 10 \text{ km s}^{-1}$ larger values than those of Shen et al. (2015b) on average. The root-mean-square (RMS) scatter around this offset is $\sim 40 \text{ km s}^{-1}$, while the typical measurement error is $\sim 15 \text{ km s}^{-1}$ in the both stud-

ies.¹² Our decomposition procedure is not optimized for the σ_{*} measurements, since the spectral resolution of the adopted stellar library ($\sigma \sim 80 \text{ km s}^{-1}$) is not sufficiently high for this analysis; we chose this library since it covers the whole of our spectral window with a wide range of stellar parameters, which is crucial for a detailed study of the decomposed stellar emission. In contrast, the emphasis is on the most reliable σ_{*} measurements in Shen et al. (2015b), who used two dedicated routines adopting spectral libraries with high resolution ($\sigma \leq 25 \text{ km s}^{-1}$). Our fitting procedure also includes Ca H and K lines, which tend to over-estimate σ_{*} (Kormendy & Illingworth 1982; Bernardi et al. 2003; Greene & Ho 2006).

4. RESULTS

We now return to the actual spectra. The derived quasar and host properties are displayed in several parameter planes in Figures 7 and 8. Their characteristic values (medians and 68% central intervals) are also presented in Figure 9 (“Model 0”). The stellar ages cluster around $t_* = 1 \text{ Gyr}$ and show a clear deficit at less than several hundred Myr, suggesting that the galaxies have not experienced major star formation in the recent past. The absence of young stars is consistent with the relatively low SFRs (within the spectroscopic fibers), which are less than $10 M_{\odot} \text{ yr}^{-1}$ in most cases. Our results agree with those of Ho (2005) and Kim et al. (2006), who found that the SFRs in broad-line quasars at $z \leq 1$ are $\sim 10 M_{\odot} \text{ yr}^{-1}$ at most, and can be much smaller considering the contribution from AGN photoionization to lines like [O II]. On the other hand, Shi et al. (2009) report moderately higher SFRs ($\sim 10 M_{\odot} \text{ yr}^{-1}$) than ours for a small number of SDSS quasars at $z \sim 1$, based on observations of polycyclic aromatic hydrocarbon emission. At least a part of this discrepancy may be due to selection effects, as their sample is about an order of magnitude more luminous than the present sample. We stress that these

¹² Note that the two studies are not independent, since they use the same spectra for the σ_{*} measurements.

are optically-selected broad-line quasars; dust-reddened or obscured quasars are different populations (see §1) and may have much higher SFRs than those estimated here. The stellar and SMBH masses of the present sample are in the range of $10^{10} M_{\odot} < M_* < 10^{12} M_{\odot}$ and $10^7 M_{\odot} < M_{\bullet} < 10^9 M_{\odot}$, respectively, suggesting that the SDSS-RM quasars are hosted by fairly massive galaxies with massive SMBHs. Finally, Figure 7 demonstrates that objects with larger stellar fraction ($f_* > 0.5$) tend to have lower $L_{[\text{OIII}]}$ and M_{\bullet} at a given redshift, while their host properties are not significantly different from those with smaller f_* .

We checked the robustness of our analysis to the model specifics, using the seven different basic models summarized in Table 1. Models 1 and 2 assume the metallicity $Z = 0.5Z_{\odot}$ and $2.0Z_{\odot}$, respectively, while Models 3 and 4 adopt different IMFs from our default Chabrier (2003) IMF. In Models 5 and 6, the host galaxies (i.e., the stellar and ISM model components) are subject to modest dust extinction, using the Small Magellanic Cloud type extinction curve ($R_{\lambda} = A_{\lambda}/E_{B-V} = 1.39(\lambda/10000)^{-1.2}$; Prevot et al. 1984; Richards et al. 2003; Hopkins et al. 2004). We do not apply this additional dust extinction to the quasar component, since the adopted empirical quasar templates already include the mean reddening, and broad-line quasars are usually observed with little extinction (see the discussion in §3.1). Finally, Model 7 assumes twice the broadening width of the Fe II template compared to the standard model. The spectral decomposition results with these different models are displayed in Figure 9. The lower/higher metallicity leads to older/younger stellar ages, as expected from the well-known age-metallicity degeneracy, and slightly higher/lower stellar masses. The Salpeter (1955) IMF results in ~ 0.2 dex higher M_* than the Chabrier (2003) or Kroupa (2001) IMF, which reflects higher mass-to-luminosity ratios by a similar factor. Assuming a color excess of $E_{B-V} = 0.2$ or 0.5 mag results in the stellar masses and SFRs simply increasing by the corresponding extinction factors ($A_V \sim 0.6$ or 1.5 mag), while the other parameters remain nearly unchanged. The assumption of the broadening width of the Fe II template has little impact. Overall, our results are qualitatively insensitive to the specifics of the spectral models; the quasar host galaxies are characterized by intermediate stellar ages ($t_* \sim 1$ Gyr), fairly large stellar masses ($M_* \sim 10^{11} M_{\odot}$), relatively low SFRs ($\lesssim 10 M_{\odot} \text{ yr}^{-1}$ unless the dust extinction is very large), and large SMBH masses ($M_{\bullet} \sim 10^8 M_{\odot}$).

As an additional test of the reliability of the SFR estimates, we compare them with SFRs estimated with a different calibrator, using the rest-frame u -band luminosity (L_u) of the stellar component. We use the Hopkins et al. (2003) calibration to derive the L_u -based SFR:

$$\text{SFR} (M_{\odot} \text{ yr}^{-1}) = \left(\frac{L_u}{1.81 \times 10^{21} \text{ W Hz}^{-1}} \right)^{1.186}, \quad (4)$$

with L_u calculated from the decomposed host spectrum of each object, extrapolated to $\lambda < 3700 \text{ \AA}$ (i.e., outside the fitting window) with the best-fit stellar model. The $[\text{O II}]$ -based and L_u -based SFR estimates are subject to different uncertainties. As described in §3.2, the $[\text{O II}]$ -

TABLE 1
MODEL SPECIFICS.

Model	Description
0 ^a ...	Standard
1 ...	$Z = 0.5Z_{\odot}$
2 ^b ...	$Z = 2.0Z_{\odot}$
3 ...	Kroupa (2001) IMF
4 ...	Salpeter (1955) IMF
5 ...	$E_{B-V} = 0.2$ mag
6 ...	$E_{B-V} = 0.5$ mag
7 ...	$\sigma_{\text{FeII}} = 3,000 \text{ km s}^{-1}$

^aThe standard model adopts $Z = Z_{\odot}$, Chabrier (2003) IMF, $E_{B-V} = 0.0$ mag, and $\sigma_{\text{FeII}} = 1,500 \text{ km s}^{-1}$.

^bThe STELIB stellar library is replaced with MILES which has a wider coverage of stellar ages at this metallicity in the Maraston & Strömbäck (2011) models.

based SFRs may be affected by object-to-object variation of the quasar contribution. The dust extinction affects nebular lines and stellar continuum in different ways, due to the different geometry of the emission regions (Calzetti et al. 1994; Charlot & Fall 2000). Nonetheless, Figure 10 shows that the two estimates are roughly comparable, although there is a large scatter. It may not be surprising that dust has only limited effect on these estimates. As previously mentioned, past observations demonstrated that the lines of sight toward optically-selected broad-line quasar nuclei are almost dust free; the color excess is less than $E_{B-V} = 0.1$ mag in the vast majority of cases (Richards et al. 2003; Hopkins et al. 2004; Salvato et al. 2009; Matute et al. 2012; Krawczyk et al. 2014). A galaxy-wide dust screen is not likely to be present, although there could be localized dusty star-forming regions. However, the present results indicate that the host galaxies are dominated by stars with intermediate ages and are not active star formers (at least within the spectroscopic fibers). Specific SFR (SFR/M_*) is even less sensitive to dust extinction than is SFR. Our test indicates that assuming moderate extinction in the decomposition procedure (Models 5 and 6) results in the stellar mass estimates simply increasing by the corresponding extinction factors. This is because the extinction does not alter the derived stellar age and hence mass-to-luminosity ratio significantly. As a result, extinction factors in SFR and M_* are effectively cancelled out when specific SFR is derived.¹³

We emphasize that our sample is not volume limited. However, it includes most of the SDSS-RM quasars at $z < 1$, which are expected to be fairly complete down to the limiting magnitude (see §2). Most of the initial sample is successfully processed through the decomposition analysis; the fraction of objects whose results we deem unreliable ($f_* < 0.1$ or $\Delta \log M_* > 0.5$ dex) is only 18 %. We provide the decomposition results for all the 191 quasars in the electronic edition of the journal.

5. DISCUSSION

5.1. Host galaxies of unobscured quasars

¹³ Little effect of dust extinction on the derived stellar age is expected from the narrow spectral window used in the first step of the decomposition procedure ($\lambda = 3700 - 4050 \text{ \AA}$; see §3.1), in which the extinction cannot alter the spectral *slope* significantly. However, the present argument may be complicated by the fact that nebular lines and stellar continuum are affected by the extinction in different ways, as described above.

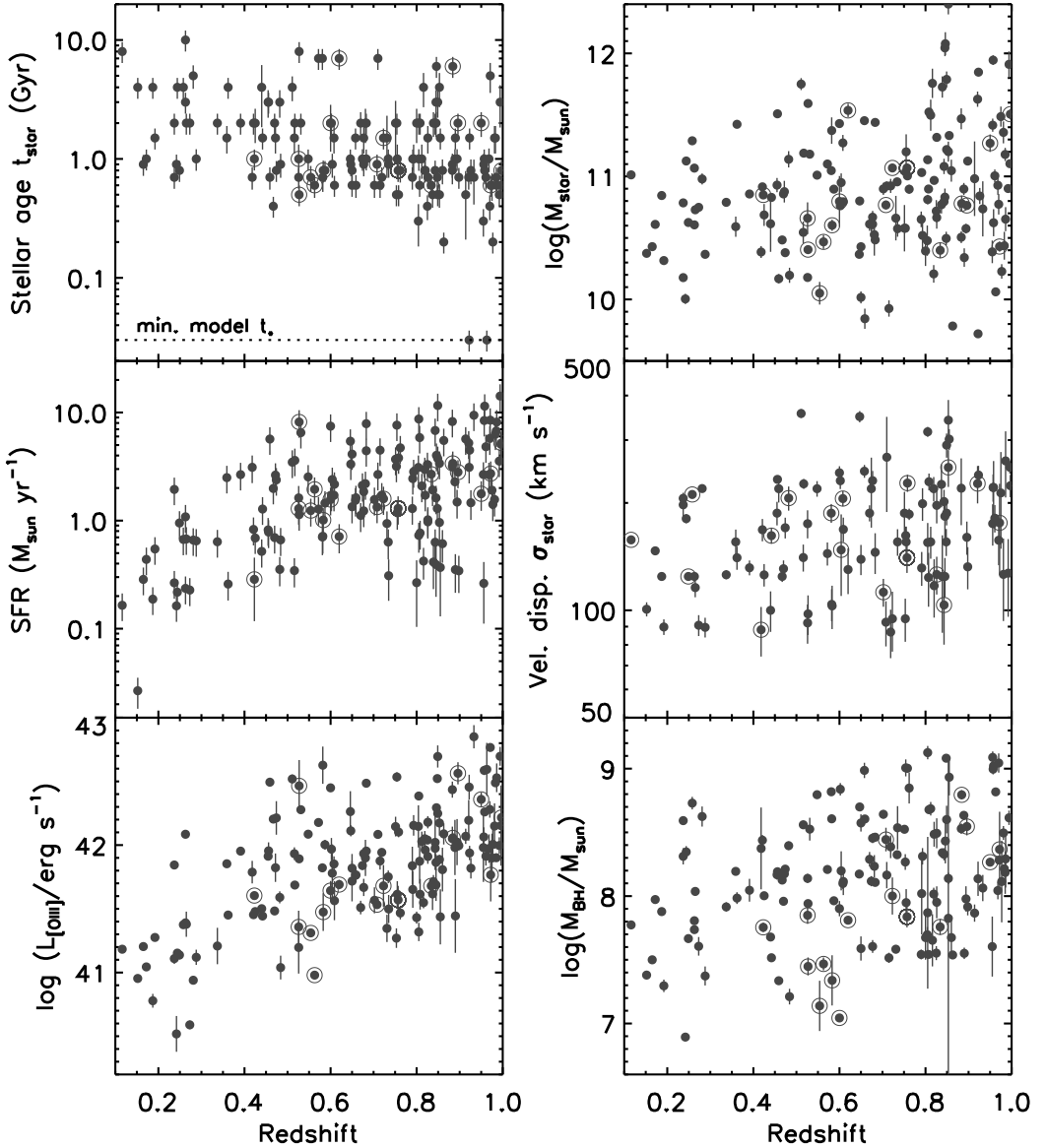


FIG. 7.— Spectral decomposition results of our sample of 156 quasars with successful measurements. Shown are t_* (top left), M_* (top right), SFR (middle left), σ_* (middle right), $L_{\text{[OIII]}}$ (bottom left), and M_\bullet (bottom right), all as a function of redshift. The objects with the stellar fraction $f_* > 0.5$ are marked with the large open circles. The error bars indicate statistical errors; there may be additional systematic uncertainties as discussed in the text. The dotted line in the top left panel represents the minimum age of our SSP models, $t_* = 30$ Myr; the two objects on this line are well fitted with this age but may have even younger stellar populations.

Before discussing the results, we first compare our measurements with those of Matsuoka et al. (2014a). They studied host galaxies of SDSS broad-line quasars at $z < 0.6$ with the imaging decomposition technique (see §1), which uses completely different data and methods from those in the present analysis. The two studies share no common objects. We calculated the host colors of the present sample by convolving the decomposed galaxy spectra (in the rest frame; they are extrapolated to $\lambda < 3700$ Å, i.e., outside our fitting window, with the best-fit stellar models) with the SDSS filter transmissions and created the CMD as shown in Figure 11. As a reference, we also plot the distribution of inactive galaxies at $0.5 < z < 1.0$ taken from the COSMOS/UltraVISTA K -band selected catalog (Muzzin et al. 2013); the rest-frame $u - r$ colors were calculated with the best-fit spectral model of each object given in the catalog. The two

measurements of the quasar hosts broadly agree in distributions of stellar mass and color, demonstrating that the quasars are preferentially hosted by massive galaxies distributed from the massive tip of the blue cloud to the red sequence. The median stellar age of the present sample, $t_* \sim 1$ Gyr, corresponds to the gap of the bimodal color distribution of inactive galaxies. It is intriguing that the quasars occupy the colors centered on this gap, where star-forming galaxies may be rapidly transitioning to the quiescent phase due to the quenching of star formation. The stellar masses of the quasar hosts ($M_* \sim 10^{11} M_\odot$) broadly agree with the turn-over mass of the local galaxy mass function at the high mass end (e.g., Bell et al. 2003). Galaxy growth is significantly suppressed above this mass (Peng et al. 2010), for which quasar activity may be playing an important role.

Figure 12 displays the relation between SFRs and stel-

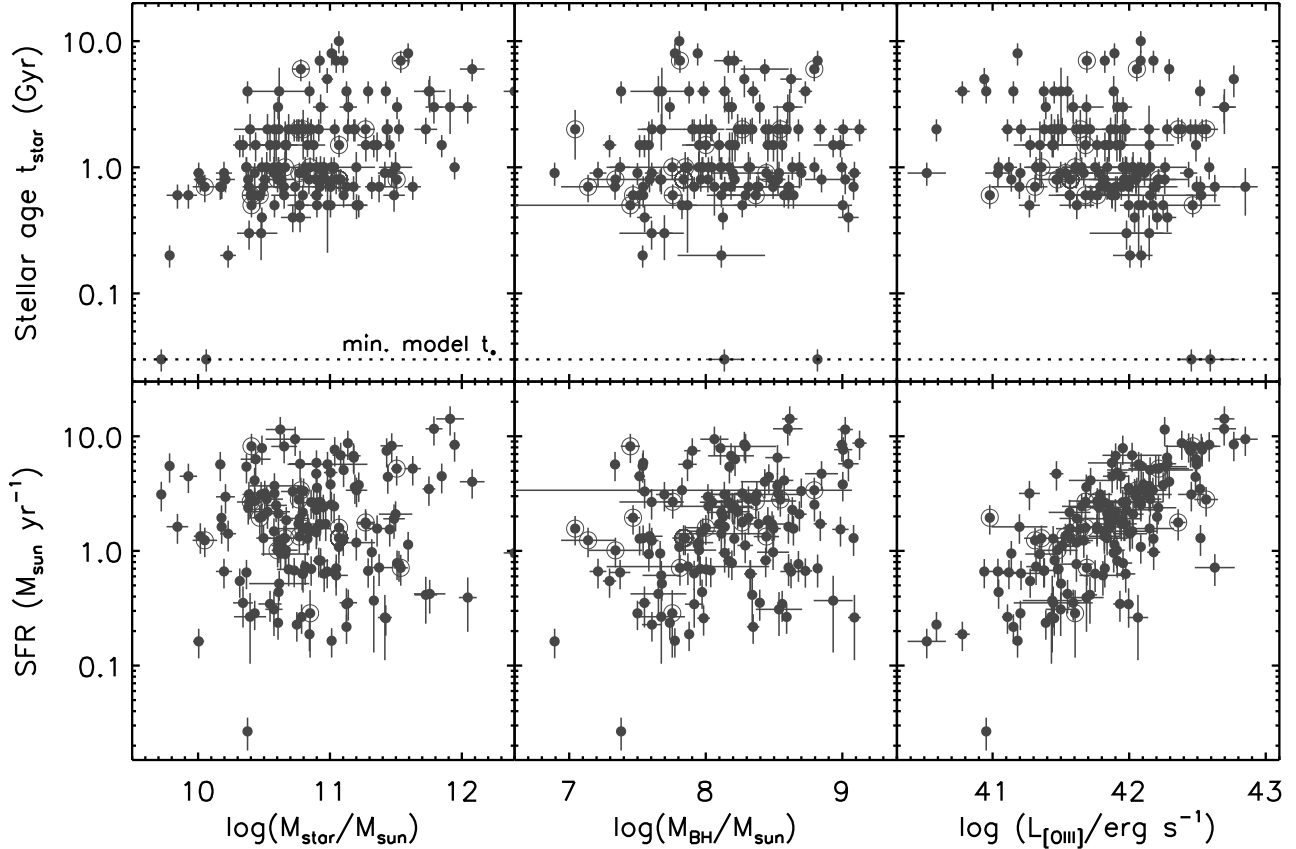


FIG. 8.— Relations between t_* (top panels) or SFR (bottom panels) and M_* (left), M_* (middle), or L_{OIII} (right). All the successful measurements of the 156 quasars are plotted. The objects with the stellar fraction $f_* > 0.5$ are marked with the large open circles. The dotted lines in the top panels represent the minimum age of our SSP models, $t_* = 30$ Myr.

lar masses within the spectroscopic fibers,¹⁴ along with the so-called “main sequence” of star-forming galaxies (e.g., Brinchmann et al. 2004; Noeske et al. 2007; Daddi et al. 2007; Elbaz et al. 2007, 2011; Steinhardt et al. 2014). The ratio between these two quantities defines specific SFR, which is not very sensitive to the dust extinction in the present analysis as discussed in §4. The majority of the quasar hosts fall below the main sequence at $z = 1$, i.e., their star formation efficiencies are considerably lower than those of normal star-forming galaxies at similar redshifts. On the other hand, SFRs measured in host galaxies of dust-obscured, X-ray selected AGNs at similar redshifts tend to be higher than estimated here and trace the main sequence of star-forming galaxies (Mullaney et al. 2012; Santini et al. 2012). However, Mullaney et al. (2015) demonstrated recently that these SFR estimates are biased toward higher values due to bright outliers in stacking analysis of infrared data, and that the actual SFR distribution of obscured AGNs is broader than, and has ~ 0.4 dex lower peak of, that of main-sequence galaxies. These findings are broadly consistent with our results for broad-line quasars presented in Figure 12.

The intermediate stellar ages and relatively low SFRs of the present sample suggest that the quasar hosts are linked to post-starburst populations. Since the first dis-

covery by Dressler & Gunn (1983), post-starburst galaxies have been recognized as an important stage of galaxy evolution. They are characterized by the presence of strong Balmer absorption lines and the absence of emission lines, which are commonly interpreted as evidence for starburst activity within the past ~ 1 Gyr, which was quenched abruptly (e.g., Quintero et al. 2004; Goto 2005). The cause of this quenching is still unknown, but the present study indicates that the formation of at least some of post-starburst galaxies is related to the nuclear activity. Quasars detected in post-starburst galaxies (e.g., Brotherton et al. 1999, 2002) may represent the relevant phase. In the Hopkins et al. (2006) merger-driven co-evolution model, a galaxy experiences various transition phases after a gas-rich merger, including a luminous infrared galaxy phase with intense star formation and dust production, an obscured AGN/quasar phase with activated central SMBHs, and an unobscured AGN/quasar phase before settling into a quiescent early-type galaxy. Our results point to the link between quasar hosts and post-starburst galaxies, suggesting that merger-induced starbursts are largely quenched before the dust obscuring the nuclear region is cleared away and the central quasar becomes optically visible. Recently Pattarakijwanich et al. (2014) estimated the number density of post-starburst galaxies to be roughly 10^{-6} $\text{Mpc}^{-3} \text{ mag}^{-1}$ for $M_{5000} > -20$ mag at $0 < z \lesssim 1$, where M_{5000} is the absolute magnitude at rest-frame 5000 Å. This value is roughly comparable to the number density of broad-line quasars at similar redshifts and luminosities

¹⁴ Here we use the stellar masses within the fibers (i.e., before the aperture correction) so that both stellar masses and SFRs refer to the same central region of the galaxies; see §3.2.

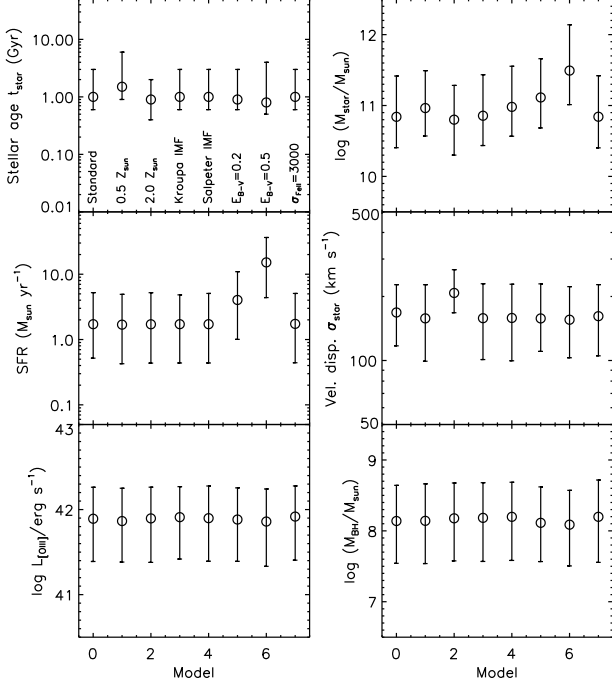


FIG. 9.— Spectral decomposition results with different model specifics as summarized in Table 1; Model 0 (standard), 1 ($Z = 0.5Z_{\odot}$), 2 ($Z = 2.0Z_{\odot}$), 3 (Kroupa IMF), 4 (Salpeter IMF), 5 ($E_{B-V} = 0.2$ mag), 6 ($E_{B-V} = 0.5$ mag), and 7 ($\sigma_{\text{FeII}} = 3000$ km s $^{-1}$). The median values (circles) and 68 % central intervals (error bars) of the derived parameter distributions are shown for t_* (top left), M_* (top right), SFR (middle left), σ_* (middle right), L_{OIII} (bottom left), and M_{\bullet} (bottom right).

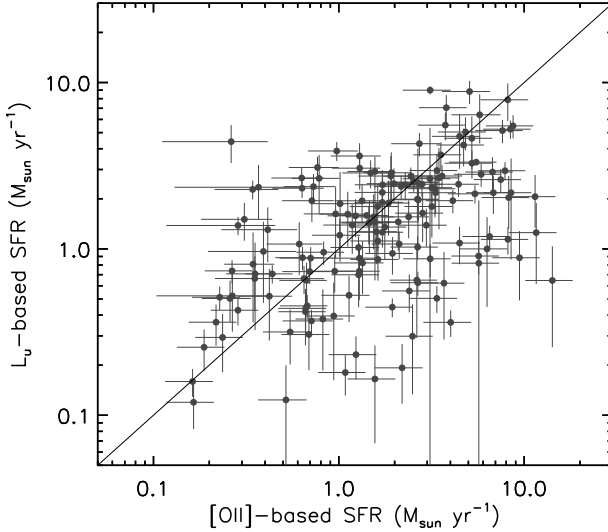


FIG. 10.— Comparison between the L_u -based and [O II]-based SFRs. The diagonal solid line represents the identity line. The two estimates are roughly comparable, although there is a large scatter.

(Richards et al. 2006; Croom et al. 2009). Kauffmann et al. (2003) noted that the strong H δ absorption observed in low- z ($z \sim 0.05$) SDSS narrow-line AGNs indicates they experienced a burst of star formation that ended within the past ~ 1 Gyr. Yesuf et al. (2014) demonstrated that the AGN fraction is three times higher in post-starburst galaxies than in inactive galaxies. However, they also reported that (obscured) AGN phase is delayed

by a few 100 Myr relative to post-starburst phase, and hence cannot play a primary role in the quenching of starbursts.

There have been a number of studies comparing the color and mass distributions of AGN host galaxies with those of inactive galaxies (e.g., Nandra et al. 2007; Salim et al. 2007; Hickox et al. 2009; Schawinski et al. 2010). Recent work suggests that, using proper mass-limited samples, the AGN fraction is constant as a function of host color, or may be enhanced in blue star-forming galaxies (e.g., Silverman et al. 2009; Aird et al. 2012; Hainline et al. 2012; Rosario et al. 2013). Luminous AGNs are preferentially found in massive host galaxies, which is perhaps due to the presence of massive SMBHs at the centers and/or of large reservoirs of gas in such galaxies. Most of these studies are based on obscured AGNs selected via their X-ray luminosity or optical narrow emission lines. Our work (Figure 11) suggests that broad-line quasar hosts prevail in the color range $1.5 < u - r < 2.5$ above masses of $\log(M_*/M_{\odot}) \sim 10.5$ and that the quasar fraction increases toward bluer colors, a trend that continues to the end of the galaxy color distribution at $u - r < 1.5$. In order to show this trend more clearly, we create a mass-matched sample of inactive galaxies; for each of the quasar hosts, the galaxy with the closest mass and redshift are drawn from the COSMOS/UltraVISTA K -band selected catalog. Figure 13 compares the histograms of the rest-frame ($u - r$) colors of the two samples. The quasar host distribution is shifted toward bluer colors than that of mass-matched inactive galaxies, demonstrating that bluer galaxies are more likely to host quasars.

Meanwhile, a drawback of the present analysis is the lack of far-infrared information and hence the dust-absorbed part of star formation. Although a galaxy-wide dust screen is unlikely to be present (see §4), the present work cannot trace localized star-forming regions hidden by dust at UV-to-optical wavelengths. Such regions can be mapped reliably only with far-infrared observations, which we will exploit in future work. Our analysis is also limited to within the spectroscopic fibers, whose 2'' diameter corresponds to approximately 14 kpc at the median redshift of the sample (see §3.2). If the majority of the star formation took place at outside this aperture, then our results would become inconsistent with the past studies which measured the entire host galaxies.

5.2. Scaling relations

Our analysis provides both stellar velocity dispersions and masses as well as SMBH masses, which allows us to investigate the scaling relations between them. Figure 14 presents the $M_{\bullet} - \sigma_*$ and $M_{\bullet} - M_*$ relations of the present sample. We calculate the linear regression lines with the IDL routine MPFITEXY, as:

$$\log\left(\frac{M_{\bullet}}{10^8 M_{\odot}}\right) = (1.64 \pm 0.29) \log\left(\frac{\sigma_*}{200 \text{ km s}^{-1}}\right) + (0.43 \pm 0.05), \quad (5)$$

and

$$\log\left(\frac{M_{\bullet}}{10^8 M_{\odot}}\right) = (0.36 \pm 0.08) \log\left(\frac{M_*}{10^{11} M_{\odot}}\right) + (0.21 \pm 0.04). \quad (6)$$

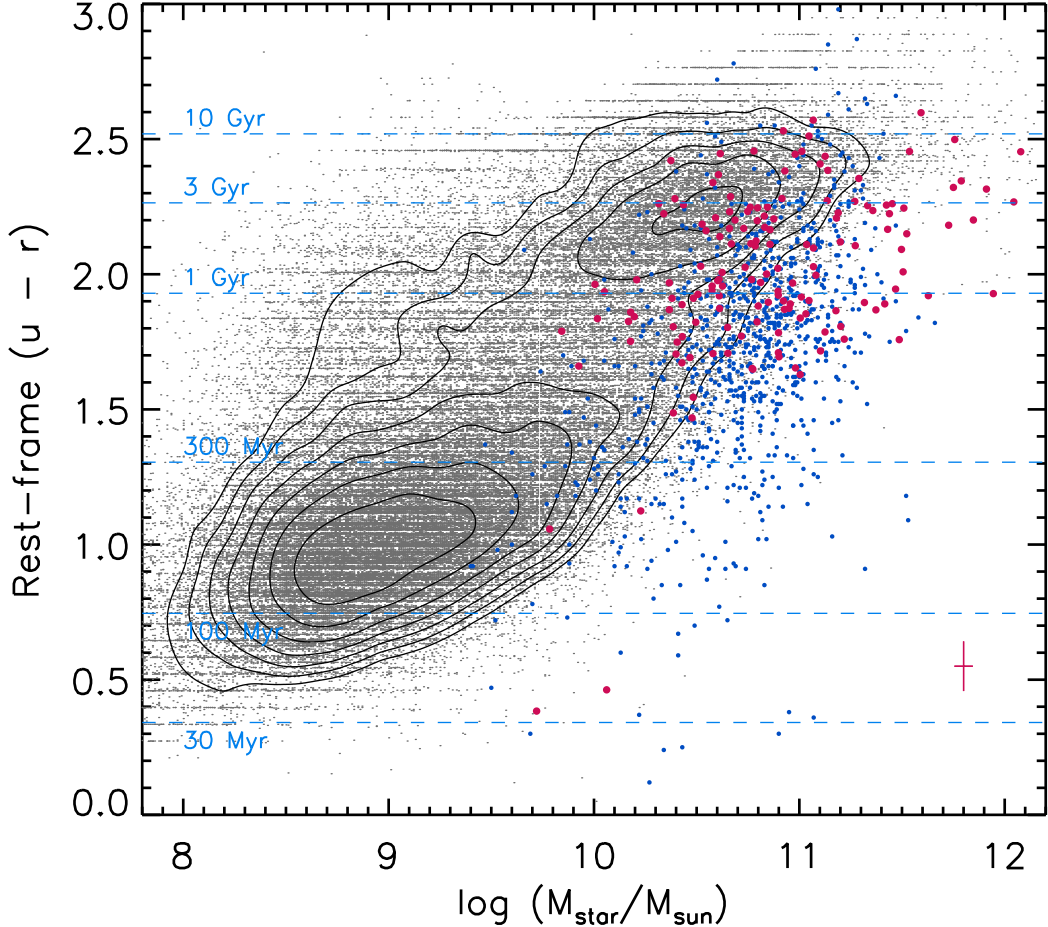


FIG. 11.— Rest-frame $(u - r)$ colors and stellar masses of the quasar host galaxies in this work (red dots) and in Matsuoka et al. (2014a, blue dots). The typical error for the present sample is shown by the error bar at the bottom right corner. The small gray dots and contours, drawn at logarithmically stepped levels of number density, represent non-AGN galaxies at $0.5 < z < 1.0$ taken from the COSMOS/UltraVISTA K -band selected catalog (Muzzin et al. 2013). The dots are given small random offsets to improve visibility. The dashed lines mark the SSP colors with $t_* = 0.03, 0.1, 0.3, 1, 3$, and 10 Gyr, as labelled. The quasar hosts are preferentially hosted by massive galaxies distributed from the massive tip of the blue cloud to the red sequence. Their mean stellar age ($t_* \sim 1$ Gyr) corresponds to the gap of the bimodal distribution of inactive galaxies, where blue star-forming galaxies may be rapidly transitioning to the red sequence.

The intrinsic scatters are 0.39 and 0.44 dex for the $M_\bullet - \sigma_*$ and $M_\bullet - M_*$ relations, respectively. The $M_\bullet - \sigma_*$ relation is almost identical to that of Shen et al. (2015b, see §3.3), which is not surprising given the consistent measurements of the two quantities (Figure 6). Our sample shows no evolution of the mean M_\bullet/σ_* ratio from the local Universe, while the slope of the relation appears to flatten toward high redshifts. This flattening was also reported by Shen et al. (2015b) and was interpreted as a result of a selection bias; with simple simulations, they concluded that a non-evolving $M_\bullet - \sigma_*$ relation is favored at $z < 1$.

We also found similar trends in the $M_\bullet - M_*$ relation. Our M_* estimates include a galaxy disk component if it is present, hence they should be regarded as the upper limits of the bulge masses ($M_{*,\text{bulge}}$). A similar comparison between the $M_\bullet - M_*$ relation at $z \sim 1.4$ and the local $M_\bullet - M_{*,\text{bulge}}$ relation was presented by Jahnke et al. (2009), who found no significant difference between the two. Since their sample shows evidence for substantial disk components, the authors concluded that bulges have grown predominantly via redistribution of the disk mass since $z = 1.4$ to the present epoch. This conclu-

sion was supported by Sun et al. (2015) with a larger sample at similar redshifts and with a careful assessment of selection biases. Our results are consistent with these findings, but we have no estimate of disk contribution to M_* and cannot provide a direct support for the above scenario. The present $M_\bullet - M_*$ relation is also similar to that of Matsuoka et al. (2014a), who reported that the relation is offset toward large M_\bullet compared to the local relation at fixed M_* . This result is likely due to the shallow slope of the relation, producing systematically large M_\bullet/M_* ratios at $M_* \lesssim 10^{11} M_\odot$.

5.3. Applicability of the present analysis

The present spectral decomposition analysis is made possible due to the low-to-moderate luminosities of the quasars, with relative stellar contribution $f_* > 0.1$ measured at $\lambda = 4000 \text{ \AA}$, and the high SNR of the spectra. Meeting both conditions usually requires significant telescope resources; in this work, we have exploited the co-added SDSS-RM spectra whose net exposure times amount to 65 hours per object. As we demonstrated in the previous sections, clear detection of stellar absorption features allows for reliable extraction of the host com-

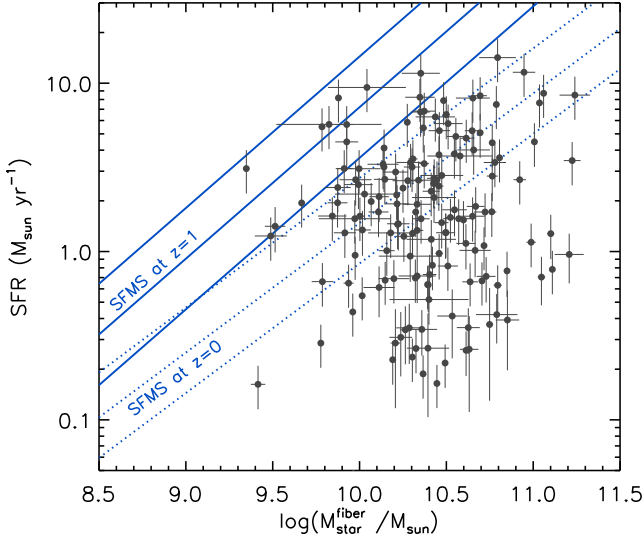


FIG. 12.— Relation between SFRs and stellar masses within the 2''-diameter spectroscopic fibers. All the successful measurements of the 156 quasars are plotted. The solid and dotted lines represent the main sequence of star-forming galaxies and their 68% confidence intervals at $z = 1$ and $z = 0$, respectively, taken from Elbaz et al. (2007). The quasar hosts fall below the main sequence, i.e., their star formation efficiencies are considerably lower than those of normal star-forming galaxies at similar redshifts.

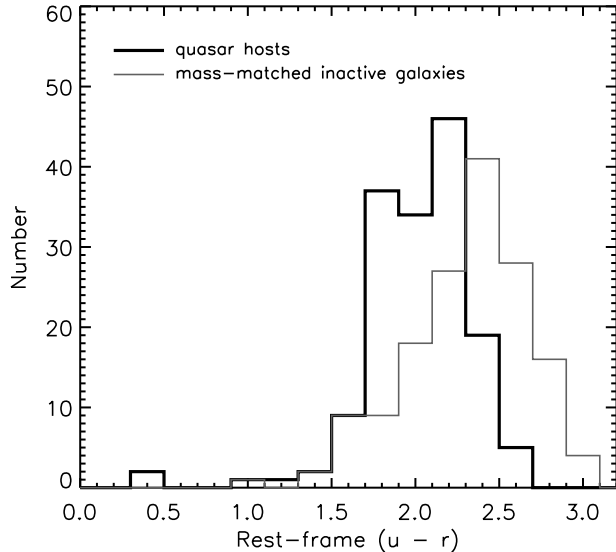


FIG. 13.— Histograms of the rest-frame ($u-r$) colors of the quasar host galaxies in this work (thick line) and the mass-matched inactive (non-AGN) galaxies drawn from the COSMOS/UltraVISTA catalog (thin line). The quasar host distribution is shifted toward bluer colors than that of inactive galaxies, demonstrating that bluer galaxies are more likely to host quasars.

ponents from the observed spectra. In this section, we give a rough guideline for estimating whether the present analysis is applicable to a given spectrum.

The first requirement is a certain fraction ($f_* \gtrsim 0.1$) of host galaxy light in the total spectrum. This fraction can be estimated roughly from the depths of the stellar absorption lines. Figure 15 presents the stellar fraction f_* as a function of EW (Ca K), the rest-frame equivalent width of the Ca K absorption line. Ca K is one of the strongest stellar absorption features in a quasar spectrum at UV-to-optical wavelengths, while Ca H is

less visible due to the superposed [Ne III] $\lambda 3969$ emission. We measure EW (Ca K) in the wavelength range $\lambda = 3920 - 3955$ Å, with the blue and red continuum levels defined at $\lambda = 3880 - 3920$ Å and $\lambda = 3990 - 4030$ Å, respectively. Figure 15 indicates that EW (Ca K) and f_* are moderately correlated. The majority of the quasars with $\text{EW} (\text{Ca K}) \gtrsim 2$ Å have more than 10% of the light at 4000 Å from the host, and stellar emission is the major contributor to a quasar spectrum on average when one observes $\text{EW} (\text{Ca K}) \gtrsim 6$ Å.

The second requirement is high SNR. We test the minimum SNR required to perform a reliable decomposition analysis by artificially degrading the SDSS-RM data and determining how the derived uncertainties change as the SNR decreases. We take the original high-SNR spectra with successful decomposition and add noise assuming a Gaussian PDF with standard deviations of 2, 4, 8, or 16 times the original pixel errors. These mock spectra are processed through the decomposition algorithm. We omit the calibration errors in Equations 1 and 2 in these simulations to view the effect of decreasing SNR directly. Figure 16 displays the resultant uncertainties in the six physical quantities as a function of the SNR per pixel measured at $\lambda = 4000$ Å. These plots can be used to infer the required SNR to achieve the desired accuracy in one of the parameters; for example, a rough estimate of stellar mass ($\Delta \log M_* < 0.5$ dex) is possible at SNR ~ 3 on average, while stellar age is poorly constrained ($\Delta t_*/t_* \sim 1$) at that SNR. All six parameters are moderately well constrained at SNR > 10 , where the actual SDSS-RM quasars are located.

6. SUMMARY

We present the results of a spectral decomposition analysis of broad-line quasars at $z < 1$. The sample is drawn from the SDSS-RM project, in which a single spectroscopic field was repeatedly observed with the BOSS spectrograph to explore the variability of quasars. The high SNR co-added spectra of 191 SDSS-RM quasars, whose net exposure times amount to approximately 65 hours per object, are used for the analysis. We develop a technique to decompose a quasar spectrum into nuclear and host components using spectral models of the quasar accretion disk, gas in the BLR, NLR, ISM, and stars in the host galaxy. This procedure provides estimates of stellar age and mass, SFR, stellar velocity dispersion, quasar [O III] luminosity, and SMBH mass, among other quantities. The decomposition was successful for more than 80 % of the initial sample; these objects have more than 10 % of their light at 4000 Å from the host, and the error in stellar mass estimates $\Delta \log (M_*/M_\odot)$ is less than 0.5. We find that the quasars are preferentially hosted by massive ($M_* \sim 10^{11} M_\odot$) galaxies with characteristic stellar ages around $t_* = 1$ Gyr. It coincides with the gap of the bimodal color distribution of inactive galaxies, where blue star-forming galaxies may be rapidly transitioning into the red sequence. The deficit of young stars is consistent with the estimated low SFRs, which place the quasar hosts below the main sequence of star-forming galaxies at similar redshifts. These facts suggest that the quasar hosts have experienced an episode of major star formation sometime in the past ~ 1 Gyr, which was subsequently quenched or suppressed (at a slower rate). We

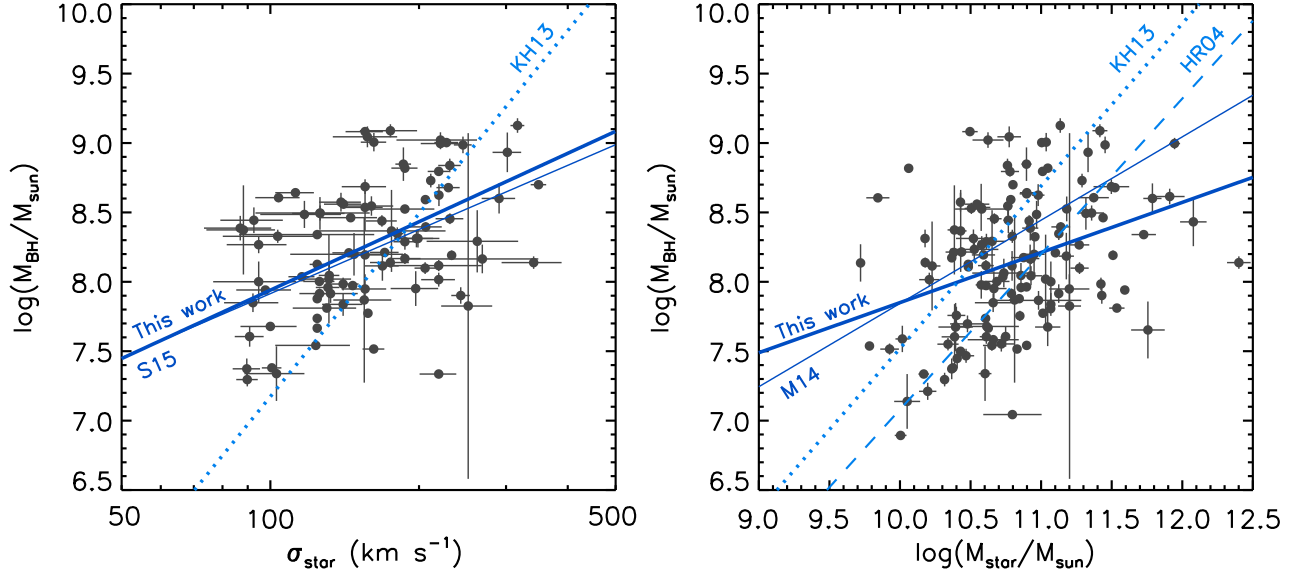


FIG. 14.— Relation between M_{\bullet} and σ_* (left) and between M_{\bullet} and M_* (right). The thick solid lines represent the regression lines of the present sample, while the thin solid lines indicate those of the previous measurements by Shen et al. (2015b, “S15”) and Matsuoka et al. (2014a,b, “M14”). The dotted and dashed lines represent the local relations taken from Kormendy & Ho (2013, “KH13”) and Häring & Rix (2004, “HR04”), respectively. Note that the KH13 and HR04 relations have been calibrated with bulge masses, while M_* of this work includes a galaxy disk component if it is present (see text). The mean M_{\bullet}/σ_* or M_{\bullet}/M_* ratio of the quasar hosts is consistent with the local value, while the slope of the relation appears to flatten toward high redshift. This flattening can be explained by selection biases (see text).

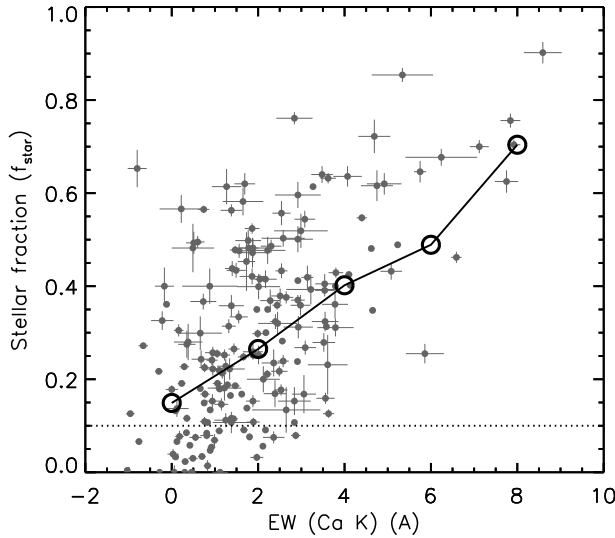


FIG. 15.— Stellar fraction (f_*) measured at $\lambda = 4000$ Å in our sample of 191 quasars, as a function of the rest-frame EW (Ca K); a positive EW value means absorption. The large circles represent median values in bins of EW (Ca K). The dotted line marks the success threshold of our decomposition analysis, $f_* > 0.1$. There is a moderate correlation between the two quantities, which allows one to make a rough estimate of f_* by measuring EW (Ca K) in a given spectrum.

also find that the scaling relations between M_{\bullet} and σ_* and between M_{\bullet} and M_* are consistent with our previous measurements. The mean M_{\bullet}/σ_* or M_{\bullet}/M_* ratio is consistent with the local value, while the slope of the relation is flatter than the local relation. As demonstrated by Shen et al. (2015b), this result is likely due to a selection bias, and no evolution of the scaling relations is favored at $z < 1$. Finally, we demonstrate that the stellar contribution to a quasar spectrum can be inferred roughly from the equivalent widths of Ca K absorption line, and pro-

vide estimates of the minimum SNR required to perform a spectral decomposition with desired precision.

The present work will be greatly advanced with future powerful spectrographs such as the Subaru Prime Focus Spectrograph (PFS; Takada et al. 2014), which will produce large numbers of high-quality spectra of galaxies and quasars out to high redshifts. Our method, optimized for BOSS fiber spectra, can be readily applied to other high-quality spectra in order to study quasars with lower luminosity and higher redshifts. It is also important to extend the present analysis into longer rest-frame wavelengths ($\lambda > 5400$ Å) with near-infrared spectrographs, where the relative host contribution becomes larger and the possible effects of dust extinction become smaller.

We are grateful to the referee for his/her useful comments and suggestions. YM thanks Nobunari Kashikawa for fruitful discussions. WNB thanks NSF grant AST-1108604 for support. LCH acknowledges support by the Chinese Academy of Science through grant No. XDB09030102 (Emergence of Cosmological Structures) from the Strategic Priority Research Program and by the National Natural Science Foundation of China through grant No. 11473002. Support for the work of YS was provided by NASA through Hubble Fellowship grant number HST-HF-51314, awarded by the Space Telescope Science Institute, which is operated by the Association of Universities for Research in Astronomy, Inc., for NASA, under contract NAS 5-26555. MYS acknowledges support from the China Scholarship Council (No. [2013]3009).

Funding for SDSS-III has been provided by the Alfred P. Sloan Foundation, the Participating Institutions, the National Science Foundation, and the U.S. Department of Energy Office of Science. The SDSS-III Web site is

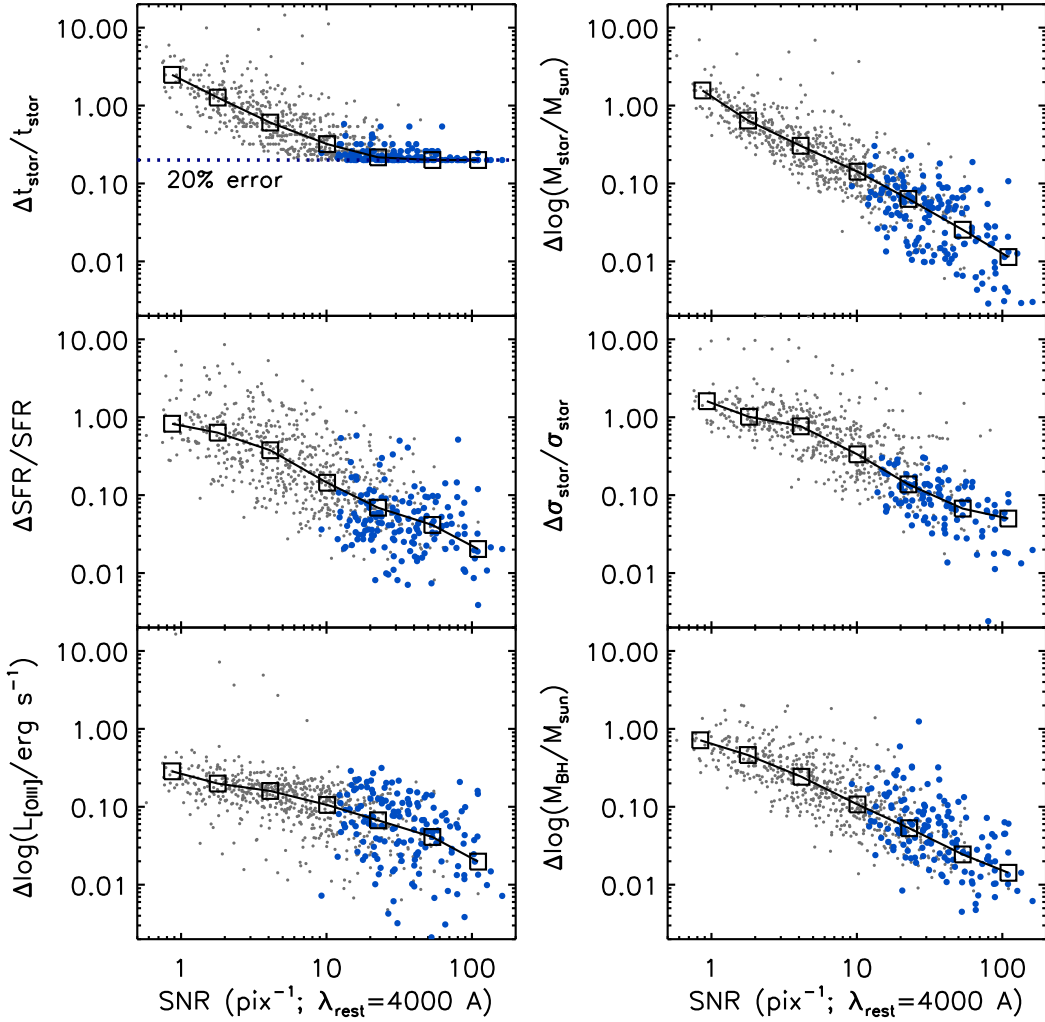


FIG. 16.— Uncertainties in t_* (top left), M_* (top right), SFR, (middle left), σ_* (middle right), L_{OIII} (bottom left), and M_\bullet (bottom right), as a function of the SNR per pixel measured at $\lambda = 4000 \text{ \AA}$. The large dots represent the original SDSS-RM spectra, while the small dots represent the mock spectra with noise added. The quantity $\Delta t_*/t_*$ has a lower limit at 0.2 (dotted line in the upper left panel) because of the 20 % error added to account for non-contiguous age coverage of the SSP models (see §3.2). The squares connected by the

<http://www.sdss3.org/>.

SDSS-III is managed by the Astrophysical Research Consortium for the Participating Institutions of the SDSS-III Collaboration including the University of Arizona, the Brazilian Participation Group, Brookhaven National Laboratory, University of Cambridge, Carnegie Mellon University, University of Florida, the French Participation Group, the German Participation Group, Harvard University, the Instituto de Astrofísica de Canarias, the Michigan State/Notre Dame/JINA Participa-

tion Group, Johns Hopkins University, Lawrence Berkeley National Laboratory, Max Planck Institute for Astrophysics, Max Planck Institute for Extraterrestrial Physics, New Mexico State University, New York University, Ohio State University, Pennsylvania State University, University of Portsmouth, Princeton University, the Spanish Participation Group, University of Tokyo, University of Utah, Vanderbilt University, University of Virginia, University of Washington, and Yale University.

REFERENCES

Abazajian, K., Adelman-McCarthy, J. K., Agüeros, M. A., et al. 2004, AJ, 128, 502

Aird, J., Coil, A. L., Moustakas, J., et al. 2012, ApJ, 746, 90

Alam, S., Albareti, F. D., Allende Prieto, C., et al. 2015, arXiv:1501.00963

Annis, J., Soares-Santos, M., Strauss, M. A., et al. 2014, ApJ, 794, 120

Bahcall, J. N., Kirhakos, S., Saxe, D. H., & Schneider, D. P. 1997, ApJ, 479, 642

Bañados, E., Venemans, B. P., Morganson, E., et al. 2014, AJ, 148, 14

Barnes, J. E., & Hernquist, L. E. 1991, ApJ, 370, L65

Bell, E. F., McIntosh, D. H., Katz, N., & Weinberg, M. D. 2003, ApJS, 149, 289

Bernardi, M., Sheth, R. K., Annis, J., et al. 2003, AJ, 125, 1817

Bolton, A. S., Schlegel, D. J., Aubourg, É., et al. 2012, AJ, 144, 144

Boroson, T. A., & Oke, J. B. 1982, Nature, 296, 397

Bower, R. G., Benson, A. J., Malbon, R., et al. 2006, MNRAS, 370, 645

Brandt, W. N., & Alexander, D. M. 2015, A&A Rev., 23, 1

Brinchmann, J., Charlot, S., White, S. D. M., et al. 2004, MNRAS, 351, 1151

Brotherton, M. S., Grabelsky, M., Canalizo, G., et al. 2002, *PASP*, 114, 593

Brotherton, M. S., van Breugel, W., Stanford, S. A., et al. 1999, *ApJ*, 520, L87

Calzetti, D., Kinney, A. L., & Storchi-Bergmann, T. 1994, *ApJ*, 429, 582

Canalizo, G., & Stockton, A. 2013, *ApJ*, 772, 132

Cano-Díaz, M., Maiolino, R., Marconi, A., et al. 2012, *A&A*, 537, L8

Cappellari, M., & Emsellem, E. 2004, *PASP*, 116, 138

Cardamone, C. N., Urry, C. M., Schawinski, K., et al. 2010, *ApJ*, 721, L38

Chabrier, G. 2003, *PASP*, 115, 763

Charlot, S., & Fall, S. M. 2000, *ApJ*, 539, 718

Choi, J.-H., & Nagamine, K. 2011, *MNRAS*, 410, 2579

Comastri, A., Gilli, R., Marconi, A., Risaliti, G., & Salvati, M. 2015, *A&A*, 574, L10

Croom, S. M., Richards, G. T., Shanks, T., et al. 2009, *MNRAS*, 399, 1755

Croton, D. J., Springel, V., White, S. D. M., et al. 2006, *MNRAS*, 365, 11

Daddi, E., Dickinson, M., Morrison, G., et al. 2007, *ApJ*, 670, 156

Davé, R., Oppenheimer, B. D., & Finlator, K. 2011, *MNRAS*, 415, 11

Dawson, K. S., Schlegel, D. J., Ahn, C. P., et al. 2013, *AJ*, 145, 10

Di Matteo, T., Springel, V., & Hernquist, L. 2005, *Nature*, 433, 604

DiPompeo, M. A., Myers, A. D., Hickox, R. C., Geach, J. E., & Hainline, K. N. 2014, *MNRAS*, 442, 3443

DiPompeo, M. A., Myers, A. D., Hickox, R. C., et al. 2015, *MNRAS*, 446, 3492

Dressler, A. 1989, Active Galactic Nuclei: proceedings of IAUS 134, held in Santa Cruz, California, August 15-19, 1988. Edited by Donald E. Osterbrock and Joseph S. Miller. IAUS 134, Kluwer Academic Publishers, Dordrecht, p.217

Dressler, A., & Gunn, J. E. 1983, *ApJ*, 270, 7

Dunlop, J. S., McLure, R. J., Kukula, M. J., et al. 2003, *MNRAS*, 340, 1095

Elbaz, D., Daddi, E., Le Borgne, D., et al. 2007, *A&A*, 468, 33

Elbaz, D., Dickinson, M., Hwang, H. S., et al. 2011, *A&A*, 533, AA119

Elitzur, M. 2012, *ApJ*, 747, L33

Eisenstein, D. J., Weinberg, D. H., Agol, E., et al. 2011, *AJ*, 142, 72

Fabian, A. C. 2012, *ARA&A*, 50, 455

Fan, X., Strauss, M. A., Becker, R. H., et al. 2006, *AJ*, 132, 117

Ferrara, A., Salvadori, S., Yue, B., & Schleicher, D. 2014, *MNRAS*, 443, 2410

Ferrarese, L., & Merritt, D. 2000, *ApJ*, 539, L9

Feruglio, C., Maiolino, R., Piconcelli, E., et al. 2010, *A&A*, 518, L155

Francis, P. J. 1996, *PASA*, 13, 212

Fu, H., & Stockton, A. 2009, *ApJ*, 690, 953

Fukugita, M., Ichikawa, T., Gunn, J. E., et al. 1996, *AJ*, 111, 1748

Ganguly, R., Brotherton, M. S., Cales, S., et al. 2007, *ApJ*, 665, 990

Gebhardt, K., Bender, R., Bower, G., et al. 2000, *ApJ*, 539, L13

Georgakakis, A., Nandra, K., Yan, R., et al. 2008, *MNRAS*, 385, 2049

Glikman, E., Urrutia, T., Lacy, M., et al. 2012, *ApJ*, 757, 51

Gofford, J., Reeves, J. N., Tombesi, F., et al. 2013, *MNRAS*, 430, 60

Goto, T. 2005, *MNRAS*, 357, 937

Greene, J. E., & Ho, L. C. 2006, *ApJ*, 641, 117

Greene, J. E., & Ho, L. C. 2005, *ApJ*, 627, 721

Greene, J. E., Zakamska, N. L., Ho, L. C., & Barth, A. J. 2011, *ApJ*, 732, 9

Gültekin, K., Richstone, D. O., Gebhardt, K., et al. 2009, *ApJ*, 698, 198

Gunn, J. E., Siegmund, W. A., Mannery, E. J., et al. 2006, *AJ*, 131, 2332

Hainline, K. N., Shapley, A. E., Greene, J. E., et al. 2012, *ApJ*, 760, 74

Hao, L., Strauss, M. A., Fan, X., et al. 2005, *AJ*, 129, 1795

Häring, N., & Rix, H.-W. 2004, *ApJ*, 604, L89

Hewett, P. C., & Wild, V. 2010, *MNRAS*, 405, 2302

Hickox, R. C., Jones, C., Forman, W. R., et al. 2009, *ApJ*, 696, 891

Ho, L. C. 2009, *ApJ*, 699, 638

Ho, L. C. 2005, *ApJ*, 629, 680

Hopkins, A. M., Miller, C. J., Nichol, R. C., et al. 2003, *ApJ*, 599, 971

Hopkins, P. F., Hernquist, L., Cox, T. J., et al. 2006, *ApJS*, 163, 1

Hopkins, P. F., Richards, G. T., & Hernquist, L. 2007, *ApJ*, 654, 731

Hopkins, P. F., Strauss, M. A., Hall, P. B., et al. 2004, *AJ*, 128, 1112

Husemann, B., Sánchez, S. F., Wisotzki, L., et al. 2010, *A&A*, 519, A115

Ivezić, Ž., Menou, K., Knapp, G. R., et al. 2002, *AJ*, 124, 2364

Jahnke, K., Bongiorno, A., Brusa, M., et al. 2009, *ApJ*, 706, L215

Jahnke, K., Sánchez, S. F., Wisotzki, L., et al. 2004, *ApJ*, 614, 568

Jahnke, K., Wisotzki, L., Courbin, F., & Letawe, G. 2007, *MNRAS*, 378, 23

Jiang, L., Fan, X., Bian, F., et al. 2009, *AJ*, 138, 305

Jiang, L., Fan, X., Vestergaard, M., et al. 2007, *AJ*, 134, 1150

Kaiser, N., Burgett, W., Chambers, K., et al. 2010, *Proc. SPIE*, 7733, 77330E

Kauffmann, G., Heckman, T. M., Tremonti, C., et al. 2003, *MNRAS*, 346, 1055

Keel, W. C., Chojnowski, S. D., Bennert, V. N., et al. 2012, *MNRAS*, 420, 878

Kennicutt, R. C., Jr. 1998, *ARA&A*, 36, 189

Kewley, L. J., Dopita, M. A., Sutherland, R. S., Heisler, C. A., & Trevena, J. 2001, *ApJ*, 556, 121

Kim, M., Ho, L. C., & Im, M. 2006, *ApJ*, 642, 702

Kirhakos, S., Bahcall, J. N., Schneider, D. P., & Kristian, J. 1999, *ApJ*, 520, 67

Kormendy, J. 1993, The Nearest Active Galaxies, Proceedings of the meeting on The nearest active galaxies, held in Madrid in May 1992, Madrid: Consejo Superior de Investigaciones Científicas, 1993, Edited by J. Beckman, L. Colina and H. Netzer, p. 197

Kormendy, J., & Ho, L. C. 2013, *ARA&A*, 51, 511

Kormendy, J., & Illingworth, G. 1982, *ApJ*, 256, 460

Kotilainen, J. K., & Ward, M. J. 1994, *MNRAS*, 266, 953

Krawczyk, C. M., Richards, G. T., Gallagher, S. C., et al. 2014, arXiv:1412.7039

Kroupa, P. 2001, *MNRAS*, 322, 231

Lacy, M., Ridgway, S. E., Gates, E. L., et al. 2013, *ApJS*, 208, 24

Le Borgne, J.-F., Bruzual, G., Pelló, R., et al. 2003, *A&A*, 402, 433

Liu, G., Zakamska, N. L., Greene, J. E., Nesvadba, N. P. H., & Liu, X. 2013, *MNRAS*, 436, 2576

Liu, G., Zakamska, N. L., Greene, J. E., Nesvadba, N. P. H., & Liu, X. 2013, *MNRAS*, 430, 2327

Liu, X., Zakamska, N. L., Greene, J. E., et al. 2009, *ApJ*, 702, 1098

Madau, P., Haardt, F., & Dotti, M. 2014, *ApJ*, 784, LL38

Magorrian, J., Tremaine, S., Richstone, D., et al. 1998, *AJ*, 115, 2285

Maraston, C., & Strömbäck, G. 2011, *MNRAS*, 418, 2785

Marconi, A., Risaliti, G., Gilli, R., et al. 2004, *MNRAS*, 351, 169

Markwardt, C. B. 2009, Astronomical Data Analysis Software and Systems XVIII, 411, 251

Matsuoka, Y. 2012, *ApJ*, 750, 54

Matsuoka, Y., Strauss, M. A., Price, T. N., III, & DiDonato, M. S. 2014a, *ApJ*, 780, 162

Matsuoka, Y., Strauss, M. A., Price, T. N., III, & DiDonato, M. S. 2014b, *ApJ*, 789, 91

Matute, I., Márquez, I., Masegosa, J., et al. 2012, *A&A*, 542, AA20

McLure, R. J., & Dunlop, J. S. 2002, *MNRAS*, 331, 795

McLure, R. J., Kukula, M. J., Dunlop, J. S., et al. 1999, *MNRAS*, 308, 377

McNamara, B. R., & Nulsen, P. E. J. 2007, *ARA&A*, 45, 117

Merritt, D., & Ferrarese, L. 2001, *MNRAS*, 320, L30

Mortlock, D. J., Warren, S. J., Venemans, B. P., et al. 2011, *Nature*, 474, 616

Mullaney, J. R., Alexander, D. M., Aird, J., et al. 2015, arXiv:1506.05459

Mullaney, J. R., Pannella, M., Daddi, E., et al. 2012, *MNRAS*, 419, 95

Muzzin, A., Marchesini, D., Stefanon, M., et al. 2013, *ApJS*, 206, 8

Nandra, K., Georgakakis, A., Willmer, C. N. A., et al. 2007, *ApJ*, 660, L11

Nesvadba, N. P. H., Lehnert, M. D., Eisenhauer, F., et al. 2006, *ApJ*, 650, 693

Netzer, H. 2015, arXiv:1505.00811

Newman, J. A., Cooper, M. C., Davis, M., et al. 2013, *ApJS*, 208, 5

Noeske, K. G., Weiner, B. J., Faber, S. M., et al. 2007, *ApJ*, 660, L43

Oke, J. B., & Gunn, J. E. 1983, *ApJ*, 266, 713

Osterbrock, D. E., & Pogge, R. W. 1985, *ApJ*, 297, 166

Pâris, I., Petitjean, P., Aubourg, É., et al. 2014, *A&A*, 563, A54

Pattarakijwanich, P., Strauss, M. A., Ho, S., & Ross, N. P. 2014, arXiv:1410.7394

Pei, Y. C. 1992, *ApJ*, 395, 130

Peng, Y.-j., Lilly, S. J., Kovač, K., et al. 2010, *ApJ*, 721, 193

Pentericci, L., Rix, H.-W., Prada, F., et al. 2003, *A&A*, 410, 75

Prevot, M. L., Lequeux, J., Prevot, L., Maurice, E., & Rocca-Volmerange, B. 1984, *A&A*, 132, 389

Pounds, K. A., Reeves, J. N., King, A. R., et al. 2003, *MNRAS*, 345, 705

Quintero, A. D., Hogg, D. W., Blanton, M. R., et al. 2004, *ApJ*, 602, 190

Reeves, J. N., O'Brien, P. T., Braito, V., et al. 2009, *ApJ*, 701, 493

Reyes, R., Zakamska, N. L., Strauss, M. A., et al. 2008, *AJ*, 136, 2373

Richards, G. T., Hall, P. B., Vanden Berk, D. E., et al. 2003, *AJ*, 126, 1131

Richards, G. T., Strauss, M. A., Fan, X., et al. 2006, *AJ*, 131, 2766

Richstone, D. O., & Schmidt, M. 1980, *ApJ*, 235, 361

Rönnback, J., van Groningen, E., Wanders, I., Örndahl, E. 1996, *MNRAS*, 283, 282

Rosario, D. J., Mozena, M., Wuyts, S., et al. 2013, *ApJ*, 763, 59

Ross, N. P., Myers, A. D., Sheldon, E. S., et al. 2012, *ApJS*, 199, 3

Salim, S., Rich, R. M., Charlton, S., et al. 2007, *ApJS*, 173, 267

Salpeter, E. E. 1955, *ApJ*, 121, 161

Salvato, M., Hasinger, G., Ilbert, O., et al. 2009, *ApJ*, 690, 1250

Sanders, D. B., Soifer, B. T., Elias, J. H., et al. 1988, *ApJ*, 325, 74

Santini, P., Rosario, D. J., Shao, L., et al. 2012, *A&A*, 540, A109

Schawinski, K., Urry, C. M., Virani, S., et al. 2010, *ApJ*, 711, 284

Schlegel, D. J., Finkbeiner, D. P., & Davis, M. 1998, *ApJ*, 500, 525

Schmidt, M., & Green, R. F. 1983, *ApJ*, 269, 352

Schneider, D. P., Richards, G. T., Hall, P. B., et al. 2010, *AJ*, 139, 2360

Schulze, A., & Wisotzki, L. 2011, *A&A*, 535, A87

Sersic, J. L. 1968, Cordoba, Argentina: Observatorio Astronomico, 1968

Shen, Y. 2013, *Bulletin of the Astronomical Society of India*, 41, 61

Shen, Y., Brandt, W. N., Dawson, K. S., et al. 2015, *ApJS*, 216, 4

Shen, Y., Greene, J. E., Ho, L. C., et al. 2015, arXiv:1502.01034

Shen, Y., & Liu, X. 2012, *ApJ*, 753, 125

Shen, Y., Richards, G. T., Strauss, M. A., et al. 2011, *ApJS*, 194, 45

Shi, Y., Rieke, G. H., Ogle, P., Jiang, L., & Diamond-Stanic, A. M. 2009, *ApJ*, 703, 1107

Silverman, J. D., Lamareille, F., Maier, C., et al. 2009, *ApJ*, 696, 396

Silverman, J. D., Mainieri, V., Lehmer, B. D., et al. 2008, *ApJ*, 675, 1025

Smee, S. A., Gunn, J. E., Uomoto, A., et al. 2013, *AJ*, 146, 32

Soltan, A. 1982, *MNRAS*, 200, 115

Somerville, R. S., Hopkins, P. F., Cox, T. J., Robertson, B. E., & Hernquist, L. 2008, *MNRAS*, 391, 481

Springel, V., Di Matteo, T., & Hernquist, L. 2005, *ApJ*, 620, L79

Steinhardt, C. L., Speagle, J. S., Capak, P., et al. 2014, *ApJ*, 791, L25

Sun, M., Trump, J. R., Brandt, W. N., et al. 2015, *ApJ*, 802, 14

Takada, M., Ellis, R. S., Chiba, M., et al. 2014, *PASJ*, 66, R1

Tombesi, F., Cappi, M., Reeves, J. N., et al. 2010, *A&A*, 521, A57

Trump, J. R., Hall, P. B., Reichard, T. A., et al. 2006, *ApJS*, 165, 1

Trump, J. R., Hsu, A. D., Fang, J. J., et al. 2013, *ApJ*, 763, 133

Trump, J. R., Sun, M., Zeimann, G. R., et al. 2015, arXiv:1501.02801

Urrutia, T., Lacy, M., & Becker, R. H. 2008, *ApJ*, 674, 80

Vanden Berk, D. E., Richards, G. T., Bauer, A., et al. 2001, *AJ*, 122, 549

Vanden Berk, D. E., Shen, J., Yip, C.-W., et al. 2006, *AJ*, 131, 84

Véron-Cetty, M.-P., Joly, M., & Véron, P. 2004, *A&A*, 417, 515

Vestergaard, M., & Peterson, B. M. 2006, *ApJ*, 641, 689

Wang, R., Carilli, C. L., Neri, R., et al. 2010, *ApJ*, 714, 699

Willott, C. J., Delorme, P., Reylé, C., et al. 2010, *AJ*, 139, 906

Wu, X.-B., Wang, F., Fan, X., et al. 2015, *Nature*, 518, 512

Xue, Y. Q., Brandt, W. N., Luo, B., et al. 2010, *ApJ*, 720, 368

Yesuf, H. M., Faber, S. M., Trump, J. R., et al. 2014, *ApJ*, 792, 84

York, D. G., Adelman, J., Anderson, J. E., Jr., et al. 2000, *AJ*, 120, 1579

Yu, Q., & Tremaine, S. 2002, *MNRAS*, 335, 965

Zakamska, N. L., Gómez, L., Strauss, M. A., & Krolik, J. H. 2008, *AJ*, 136, 1607

Zakamska, N. L., Strauss, M. A., Krolik, J. H., et al. 2006, *AJ*, 132, 1496

Zakamska, N. L., Strauss, M. A., Krolik, J. H., et al. 2003, *AJ*, 126, 2125